

Dynamics of Ringed Barred Spiral Galaxies. I. Surface Photometry and
Kinematics of NGC 1433 and NGC 6300

Ronald J. Buta – University of Alabama

et al.

Deposited 06/21/2019

Citation of published version:

Buta, R., et al. (2001): Dynamics of Ringed Barred Spiral Galaxies. I. Surface Photometry
and Kinematics of NGC 1433 and NGC 6300. *The Astronomical Journal*, 121(1).

DOI: [10.1086/318024](https://doi.org/10.1086/318024)

DYNAMICS OF RINGED BARRED SPIRAL GALAXIES. I. SURFACE PHOTOMETRY AND KINEMATICS OF NGC 1433 AND NGC 6300

R. BUTA,^{1,2} STUART D. RYDER,^{2,3} GREGORY J. MADSEN,^{2,4} KAREN WESSON,⁵ D. A. CROCKER,^{1,2} AND F. COMBES⁶

Received 2000 July 11; accepted 2000 October 10

ABSTRACT

This paper presents new near-infrared images and surface photometry and H α Fabry-Perot radial velocities for NGC 1433 and NGC 6300, two large and previously well-studied nearby ringed barred spiral galaxies. Stellar absorption-line radial velocities and new optical surface photometry are also presented for NGC 1433. The data are intended to set the stage for dynamical modeling of the two galaxies, with the principal goals being to derive mass distributions, bar mass-to-light ratios, bar pattern speeds, and resonance locations, parameters which have been derived for very few ringed disk galaxies. The presence of strong rings and pseudorings in the two galaxies allows the possibility to link specific orbital resonances with the observed rings. The new data allow us to derive a fairly complete composite rotation curve of NGC 1433, leading us to make some interesting preliminary judgments about the structure of the galaxy. The new data also verify the previous finding that the radial velocity of the Seyfert nucleus in NGC 6300 differs from the actual systemic velocity of the galaxy by nearly 100 km s⁻¹. We demonstrate in this paper that the offset is *not* an artifact of significant extinction in the inner regions of the galaxy.

Key words: galaxies: individual (NGC 1433, NGC 6300) — galaxies: kinematics and dynamics — galaxies: structure

1. INTRODUCTION

Ringed disk galaxies are an important subgroup of the barred spiral galaxy population. Rings are thought to form by gas accumulation at resonances, under the continuous action of gravity torques from the bar pattern (Buta & Combes 1996). This association with orbital resonances makes rings in barred galaxies useful tracers of internal dynamics, and given the relative abundance of rings in barred galaxies, means that studies of ringed galaxies could shed light on the dynamics of the disk galaxy population as a whole. However, very few ringed barred galaxies have ever been the subject of a detailed dynamical analysis. An exception is IC 4214, for which a successful model was obtained by Salo et al. (1999). Dynamical models can be used to derive not only the mass distribution in a ringed barred spiral, but also the pattern speed of the bar and the location of corotation relative to the ends of the bar. Such models can also be used to test the idea that rings are connected with specific orbital resonances with the bar. Since bar pattern speeds are one of the fundamental unknowns of galaxy dynamics, studies of ringed galaxies could be particularly useful for determining trends in this parameter.

In this paper, we set the stage for a dynamical analysis of two large and somewhat dissimilar ringed barred disk gal-

axies, NGC 1433 and NGC 6300. Our goals are to simulate the structure of these galaxies using a test-particle code and from the simulations derive the pattern speed of the bar, the locations of orbital resonances, and the mass-to-light ratio of the bar. Here all we do is present the supporting observational data needed for the simulations. This includes new Fabry-Perot velocity fields, near-infrared images, long-slit spectroscopy, and new optical surface photometry. The simulations will be presented in Buta & Combes 2001 (Paper II). A preliminary discussion of these simulations is provided by Buta & Combes (2000).

2. SUMMARY OF PREVIOUS OBSERVATIONS OF NGC 1433 AND 6300

The galaxies we analyze here are well studied, excellent examples of ringed barred spiral galaxies. NGC 1433 is a classic “theta” spiral first studied in great detail by Buta (1986, hereafter B86). It is the nearest example of a ringed barred spiral of de Vaucouleurs type SB(rs)ab. The inner ring in this case is actually a pseudoring made up of tightly wrapped spiral arms that wind into an oval shape aligned along the bar axis. The galaxy also has an outer pseudoring about twice the diameter of the bar and a nuclear ring about 0.1 times the diameter of the bar. Just beyond the inner ring, on the leading sides of the bar, the galaxy also shows two striking partial spiral arcs (“plumes”) that are rarely seen in barred galaxies (Buta 1984).

Other early studies of NGC 1433 include that of Baumgart & Peterson (1986), who presented some photographic information on the near-infrared properties of the bar and noted isophote twisting in the inner regions and a Freeman (1970) type II exponential disk profile. Simien & de Vaucouleurs (1986) used standard decomposition techniques to derive a bulge contribution of 13% in blue light, uncertain because of the strong bar. Harnett (1987) mapped the radio continuum emission from NGC 1433 and found a slight elongation of emission along the bar axis. Maia, da Costa, & Latham (1989) have placed NGC 1433 into a large group

¹ Department of Physics and Astronomy, University of Alabama, Tuscaloosa, Alabama 35487-0324.

² Visiting Astronomer, Cerro Tololo Inter-American Observatory, National Optical Astronomy Observatories, operated by the Association of Universities for Research in Astronomy (AURA), Inc., under cooperative agreement with the National Science Foundation.

³ Anglo-Australian Observatory, P.O. Box 296, Epping, NSW 1710, Australia.

⁴ Department of Astronomy, University of Wisconsin, 475 North Charter Street, Madison, WI 53706.

⁵ School of Environment, Duke University, Box 900328, Durham, NC 27708.

⁶ DEMIRM, Observatoire de Paris, 61 Avenue de l’Observatoire, F75014 Paris, France.

(G13) including more than 40 other large, nearby southern galaxies. The mean Virgocentric velocity of the group is only 753 km s^{-1} .

NGC 6300 is a well-known Seyfert 2 galaxy (Phillips, Charles, & Baldwin 1983) and hence has been the subject of many studies. It is an excellent SB(rs)-type spiral that provides an interesting contrast with NGC 1433. First studied in global detail by Buta (1987, hereafter B87), NGC 6300 is characterized by a relatively weak bar and strong spiral inner pseudoring. On deprojecting the galaxy, B87 noticed that the inner pseudoring is misaligned with the bar axis by nearly 80° . This misalignment is unusual for ringed barred galaxies and in this case suggests the possibility that the spiral arms in the inner pseudoring have a different pattern speed from that of the bar.

The distribution and velocity field of atomic hydrogen in NGC 1433 and 6300 were obtained by Ryder et al. (1996). These observations provided well-determined estimates of the orientation parameters of the two galaxies. For NGC 1433, Ryder et al. determined a (receding) kinematic line of nodes position angle of 201° and favored an inclination of 33° based on ellipse fits to outer isophote shapes by B86. We will not be able to improve much on these estimates here, so we will adopt them for some of our analysis. For NGC 6300, Ryder et al. found evidence for warping in the outer H I disk, but in the inner optically bright part of the disk the velocities are consistent with a line of nodes position angle of 109° and an inclination of 50° , similar to values derived by B87.

3. OBSERVATIONS AND REDUCTIONS

For our analysis of these galaxies we are using three sets of data: (1) *H*-band images at $1.65 \mu\text{m}$, assumed to be dominated almost entirely by old stars and to trace the stellar mass distribution; (2) optical velocity fields from H α Fabry-Perot interferometry; and (3) the H I velocity fields. For NGC 1433, we also have stellar spectroscopy. The distances we assume are 11.6 Mpc for NGC 1433 and 14.3 Mpc for NGC 6300 (Tully 1988).

3.1. Broadband Imaging and Morphology

The *H*-band data for NGC 1433 were obtained using the CTIO infrared imager (CIRIM) attached to the CTIO 1.5 m telescope in 1996 February. Because of the galaxy's size ($D_{2.5} \approx 7'$ compared with the field of view of $5' \times 5'$) and low inclination (33°), nine positions were used to construct a mosaic image having a field of view of 9.3×9.2 . Each position involved five dithered frames based on 10 internal coadds of 6 s each. The dithering took place in a regular pattern along a box of $15''$ – $20''$ width on a side. The scale of the images is $1''.14 \text{ pixel}^{-1}$. The night was photometric and the final mosaic image was calibrated using a few standards from Elias et al. (1982).

New optical images of NGC 1433 in Johnson *B* and Cousins *I* were obtained using a TEK2 1024 \times 1024 CCD attached to the CTIO 1.5 m telescope in 1992 August. The scale of these images is $0''.434 \text{ pixel}^{-1}$. The night was photometric and the images were calibrated using standards from Landolt (1992). Total exposure times were 600 s in *B* and 250 s in *I*. Unfortunately, the field of view of these images is only 7.4×7.4 , making sky determinations difficult. We used drift scans published by B86 to judge the sky levels on both images and check calibrations.

CIRIM was used to observe NGC 6300 in 1997 July, also on the CTIO 1.5 m telescope. In this case, it was only necessary to observe two mosaic positions. At each mosaic position, we obtained two sets of five dithered frames based on 10 internal coadds of 6 s each. The final mosaic constructed has a field of view of 8.2×5.6 . Since the observations were made with some clouds present, and no *H*-band aperture photometry is available, we could not reliably calibrate this image.

3.2. Optical Fabry-Perot Interferometry

The optical velocity data of NGC 1433 and NGC 6300 were obtained in 1997 November and July with the Rutgers Fabry-Perot (RFP) interferometer attached to the CTIO 1.5 m and 4 m telescopes, respectively. The broad etalon with a full width at half-maximum (FWHM) of 2.4 \AA was used for all of the observations, and the H α line was the only emission line used for the radial velocity measurements.

For NGC 1433, the velocity interval needed to cover the velocity field into the continuum was from 830 to 1290 km s^{-1} . Two sequences of nine frames each and separated by 1.2 \AA on average were used to cover this interval. Two sequences were used because the field of view of the RFP is 7.8 at $f/7.5$ on the CTIO 1.5 m telescope, so the galaxy just fits into the field. The first sequence had the galaxy centered on the west half of the bar, while the second sequence had the galaxy centered near the east half of the bar. The two sequences gave us two separate velocity fields which are useful for internal consistency checks. Using local position standards from the STScI Guide Star Catalog, the scale of the NGC 1433 images was measured to be $0''.957 \pm 0''.001 \text{ pixel}^{-1}$, and each frame has the same exposure time of 400 s.

For NGC 6300, the small field of view of only 2.8 diameter meant that the galaxy had to be observed in mosaic fashion. Two positions were used, separated by $115''$ in right ascension and $53''$ in declination, in order to cover the whole inner section of the galaxy, including the bright inner ring. The western sequence included 13 frames while the eastern sequence included 10 frames, with a complete velocity coverage ranging from 780 to 1600 km s^{-1} . Each frame was separated by 1.2 \AA on average and had the same exposure time of 300 s. The effective spectral resolution is probably somewhat poorer than 1.2 \AA because of small zero-point shifts from frame to frame. For NGC 6300, the zero point shifted by 0.2 \AA from the beginning to the end of the sequence of frames. For NGC 1433, the shift was less than 0.1 \AA . The scale of the NGC 6300 images is $0''.348 \text{ pixel}^{-1}$. Although the observations were obtained during strongly variable cloudiness, the CTIO 4 m control system had a transparency monitoring capability that allowed us to stop and restart the integrations as needed when the transparency improved. The main consequence of the poor transparency conditions was that we do not detect with our images the faint diffuse emission in the bar region of the galaxy (see B87), thus preventing a complete coverage of the velocity field in the inner regions.

The main steps in the reduction of the images for both galaxies was removal of cosmic rays, matching of point-spread functions (PSFs) on individual frames, determination of image shifts and sky levels, normalization, calibration, and heliocentric corrections. The PSF matching was performed by estimating the FWHM of individual foreground stars on each frame and degrading the frames to the

FWHM of the poorest frame. This was performed with the Image Reduction and Analysis Facility (IRAF)⁷ routines IMEXAMINE and GAUSS. For NGC 1433, the FWHM ranged from 1".8 to 2".2, while for NGC 6300 the FWHM ranged from 1".1 to 1".7. For both galaxies, the systemic velocities are low enough that some frames contain rings caused by telluric night sky emission lines. These were removed using a program called SKYRING2.F, based on a code provided by T. Williams of Rutgers University and modified by G. Purcell (Purcell 1998). The procedure involved determination of a biweight profile from the optical axis to the edge of the camera aperture, followed by the fitting of part of this profile by a function which describes the RFP instrumental profile. In addition to night sky rings, it was also necessary to remove the light due to internal reflections within the camera, a phenomenon known as "ghosting." A bright star on one side of the optical axis can produce a secondary image on the exact opposite side of the optical axis (see, e.g., Caldwell et al. 1991). If the galaxy itself has a bright nucleus, this can also produce a troublesome ghost image. Using bright stars on the NGC 1433 and 6300 images, as well as other images obtained during the same observing runs, we determined that the ghosts are at a level of only 3.6% for the NGC 1433 images and 4.4% for the NGC 6300 images. Using these values, we subtracted ghosts from each frame on a quadrant by quadrant basis, after determining the coordinates of the optical axis. In general, this procedure worked well, and our final velocity maps are based on the ghost-corrected images.

The normalization of the frames for each galaxy was based on photometry of several foreground stars. Because of the variable transparency, normalization factors for NGC 6300 showed a large variation, with some frames reduced by a factor of nearly two compared to others. The transparency was much better during the NGC 1433 observations. The calibration of the wavelength scale was provided by observations of several neon emission lines as well as H α from calibration lamps on the first night of each observing run. The radii (ρ) of the rings due to these lines were then fitted with a function of the form

$$\lambda = \cos [\arctan (\rho/F)](A + Bz + Cz^2),$$

where z is the etalon spacing and F , A , B , and C are constants. The values of A from these solutions were not used directly because the zero point tends to slowly shift over a night, because of temperature changes and other factors. To allow for zero-point shifts, we interspersed the observations of each galaxy with single calibration ring exposures so that we could measure the value of A as a function of time during each set of observations. The zero point was then interpolated to the mean universal time of the galaxy exposures. The variation can amount to a few tenths of an angstrom.

3.3. Slit Spectroscopy

Slit spectra of NGC 1433 were obtained using the Royal Greenwich Observatory Spectrograph with the image photon counting system (IPCS) attached to the 3.9 m telescope of the Anglo-Australian Observatory on 1984

December 21. Wavelength calibration of these spectra was made from observations of a Cu-Ar lamp. The observations were made along two slit positions, one set at the photometric major-axis position angle of 17° (B86) and the other set at the bar position angle of 96° (close to the galaxy minor axis). The spectra were centered around the Mg I b lines near 5170 Å, which were popular at the time for stellar radial velocity and velocity dispersion measurements. Two K giants, HD 15322 and HD 39280, were used as template standards for these measurements. The total amount of exposure time on the galaxy was 8600 s along position angle 17° and 6000 s along position angle 96°. The spatial scale along the slit was determined to be 1".14 pixel⁻¹.

The reduction of these spectra was carried out using the IRAF package TWODSPEC. Two long flat fields of 8600 s and 9999 s duration were used to correct for pixel-to-pixel variations. Sky subtraction of the flat-fielded spectra was performed by summing individual sky frames, each of 200–250 s duration, interspersed between the galaxy observations and scaling this image according to exposure time. A blank sky field was also used to derive an illumination correction. IRAF routine APFIND was used to find the position of the nucleus on each frame.

The derivation of radial velocities and velocity dispersions was carried out using STSDAS routines FQUOT and XCOR in IRAF. FQUOT is based on the Fourier quotient method (Sargent et al. 1977), and it has been the method of choice for many velocity dispersion measurements. XCOR is based on a cross-correlation technique (Tonry & Davis 1979), and seems best for measuring radial velocities from stellar absorption lines. We will show the results from both methods in § 4.4.

4. ANALYSIS OF NGC 1433

4.1. Morphology and Surface Photometry

We show a variety of images here to add to what was determined by B86. First, the near-infrared morphology of NGC 1433 is compared with its B -band morphology in Figure 1. As expected, the H -band morphology is smoother than in B , but nevertheless the galaxy shows the same general structure. The inner ring is a stellar pseudoring at 1.6 μ m. The outer ring is more symmetric in H than in B , while the secondary spiral arcs off the ends of the bar (Buta 1984) are much less conspicuous in H compared to B . The region of the nuclear ring shows a symmetric secondary bar, already noted by B86 and Wozniak et al. (1995).

The H I/optical orientation parameters in the previous section were used to deproject our optical images of NGC 1433. Although only approximate, the deprojections give us some idea of the intrinsic properties of the rings that our models will have to account for. Figure 2 shows a deprojected B -band image and a $B-I$ color index map of NGC 1433. In both maps, the bar has been rotated to the horizontal position. These images demonstrate the extreme intrinsic elongation of the inner ring of the galaxy. Table 1 summarizes the results of new ellipse fits to the shape of this ring as well as the other features in the galaxy. The inner ring was isolated for a fit by extracting from the $B-I$ color index map pixels in the ring having $B-I < 1.6$. The other features in Table 1 were mapped visually on a monitor display, since color selection was not as effective as for the inner ring. The nuclear ring was mapped in $B-I$ while the outer pseudoring and the plumes were mapped in B . The

⁷ IRAF is distributed by the National Optical Astronomy Observatories, which is operated by AURA, under contract with the National Science Foundation.

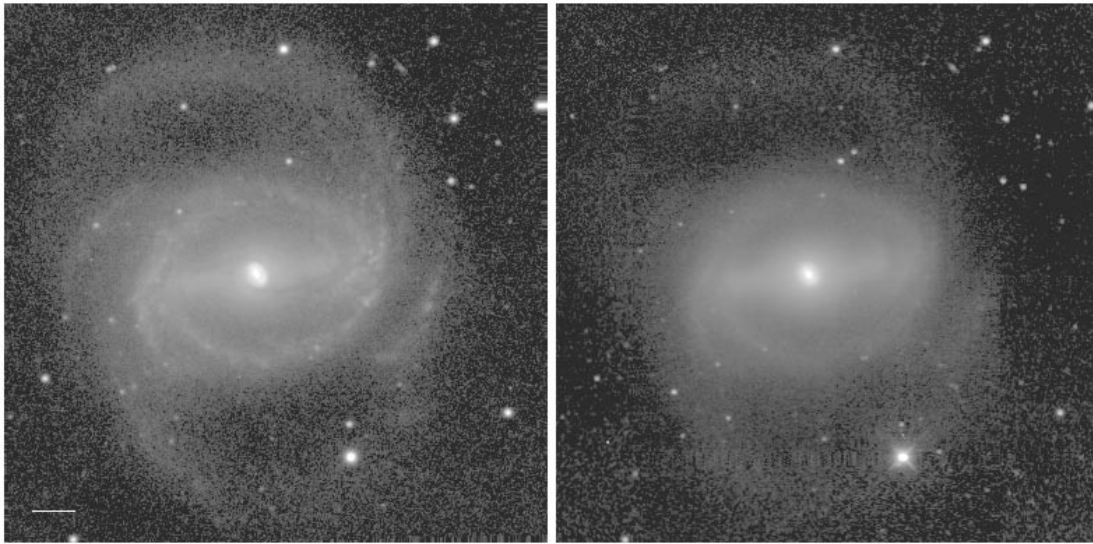


FIG. 1.—*B*-band CCD image (left) and *H*-band image (right) of NGC 1433. The images are displayed in units of magnitudes per square arcsecond from 18.0 to 27.0 in *B* and 14.0 to 23.0 in *H*. Each image covers a field of view of 7.40×7.34 . The scale bar in the lower left of the *B*-band image is 2 kpc in length. North is at the top, and east to the left.

TABLE 1
DEPROJECTED FEATURE SHAPES AND SIZES FOR
NGC 1433^a

Feature (1)	a (kpc) (2)	q (3)	θ (4)
Nuclear ring	0.5	0.90	62
Bar ^b	4.6	...	0
Inner ring	6.0	0.63	-1
Plumes	10.3	0.59	-6
Outer pseudoring	10.7	0.89	79

^a Col. (1): ring or feature; col. (2): semimajor-axis radius in kpc; col. (3): axis ratio b/a ; col. (4): angle (degrees) of fitted ellipse major axis relative to the bar. A negative value of θ means the ellipse is tipped trailing the bar, while a positive value means the ellipse leads the bar, assuming trailing spiral arms.

^b Not based on an ellipse fit. See Fig. 4a.

latter features were found to be extremely well represented as the arcs of a highly elongated ellipse oriented nearly parallel to the bar axis. The inner ring deprojects into a very elliptical feature aligned virtually exactly with the bar axis, while the outer pseudoring deprojects into a near perpendicular alignment with the bar. The size and shape of the blue nuclear ring, as well as its strong misalignment with the bar, are typical of nuclear rings (Buta & Crocker 1993).

Azimuthally averaged (Fourier component $m = 0$) surface brightness profiles were derived in all three filters and are shown in Figure 3. These are also based on the $H \ I$ /optical orientation parameters and have been used to compute new total magnitudes of NGC 1433. The magnitudes were derived by extrapolating the profiles under the ring humps as exponentials, shown by the dotted lines in Figure 3. The parameters of these exponentials are summarized in Table 2 (data sets: $m = 0$ profiles). The resulting

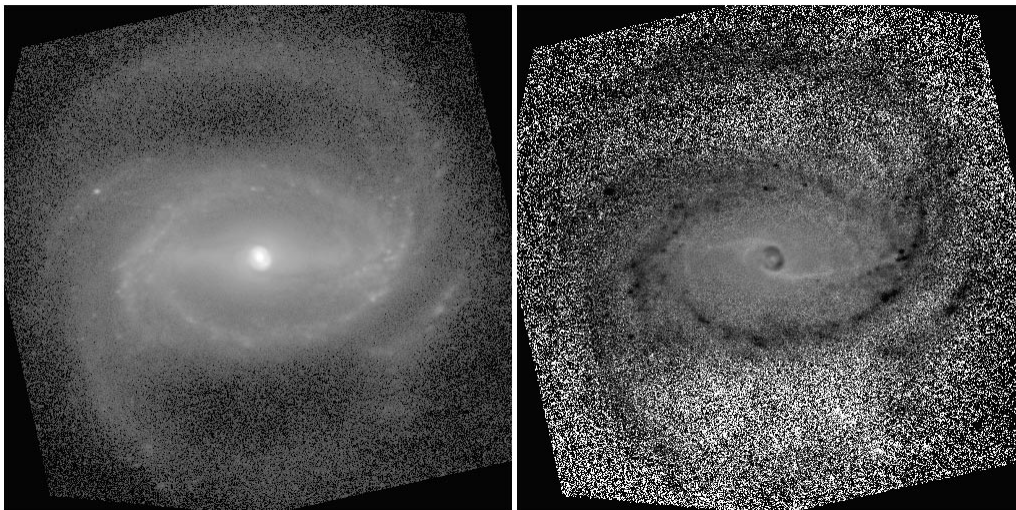


FIG. 2.—Deprojected *B* (left) and *B-I* (right) images of NGC 1433. The images are based on IRAF routine IMLINTRAN and used an inclination of 33° and a line of nodes position angle of 201° . The images are rotated such that the bar axis is horizontal. Foreground stars are removed.

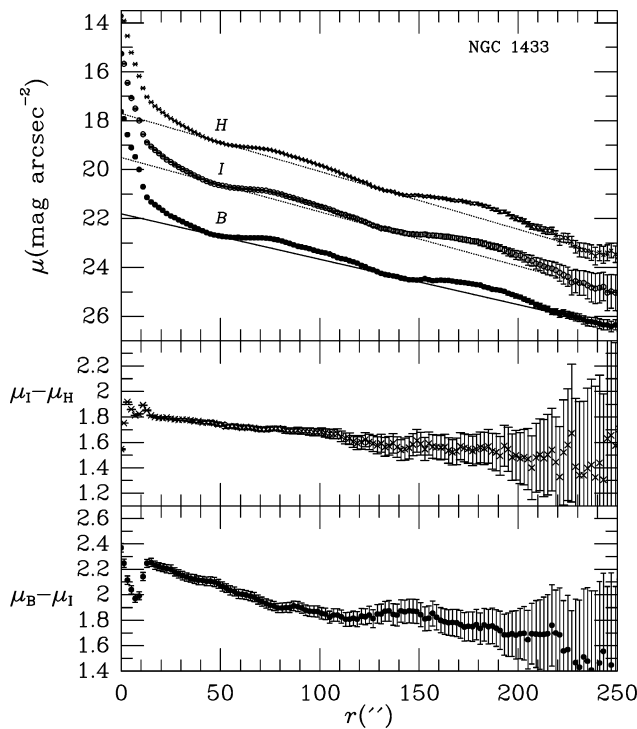


FIG. 3.—Azimuthally averaged surface brightness and color index profiles of NGC 1433, based on an inclination of 33° ($\cos i = 0.839$) and a major-axis position angle of 201° . The dotted lines are exponential fits to the background underlying the humps in the profiles (see Table 2). The decrease in $\mu_I - \mu_H$ as $r \rightarrow 0$ is due to a resolution mismatch.

magnitudes are $B_T = 10.83$, $I_T = 8.90$, and $H_T = 7.20$. The value of B_T may be compared with 10.70 derived by B86 and 10.84 derived by Lauberts & Valentijn (1989). The CCD photometry was also compared with the surface photometry provided by B86 by averaging within the ellipse defined by the photometric orientation parameters. The B and I profiles so computed agreed within ± 0.15 mag out to $250''$ with those given by B86, with better agreement found for the I -band.

4.2. Bar and Bulge Properties

We seek in this section some information on the properties of the bar and bulge in NGC 1433, such as scale lengths and central surface brightnesses, in the near-infrared. Standard bulge/disk decompositions, such as are described by

Kormendy (1977) and Simien & de Vaucouleurs (1986), are not really practical for a strongly barred galaxy such as NGC 1433. The bar of NGC 1433 is a major component in the inner regions of the galaxy. There is also a strong *lens*, a component less elongated than the bar, which appears as a plateau in the luminosity distribution perpendicular to the bar axis, followed by a sharp edge (see Fig. 9 of B86). In the bulge and bar-dominated area of the galaxy, we will treat the lens as a component of *constant* surface brightness. In this and succeeding sections *also*, we will use the coordinate x_b to denote a radial coordinate along the bar axis in the galaxy plane, measured on a deprojected image. The coordinate y_b will denote a deprojected distance from the bar axis measured along a line perpendicular to the bar. The letter r will be used to denote a radius in the sky plane, measured on a nondeprojected image, while R will be a general radius in the galaxy plane.

The bulge is a complex feature in NGC 1433. As we will show in § 4.5, the inner part of the bulge is probably as highly flattened as the disk. However, bulge isophotes appear to be rounder at larger radii, suggesting a possibly spherical or less flattened component. Our procedure to extract the light profile of this component was to try and model the bar light distribution along its minor axis, in order to remove the bar. No standard assumptions about the bulge and disk (such as $r^{1/4}$ bulge or exponential disk) are made in the analysis; instead, the bar and bulge are assumed to be within the lens and hence in an area of constant background surface brightness. Our cleaned, sky-subtracted H -band image was first deprojected using IRAF routine IMLINTRAN assuming a line of nodes position angle of 201° and an inclination of 33° . The resulting image placed the line of nodes along the horizontal position, and in this image the bar has a position angle of 168.2° . The folded H -band light profile along this axis is shown in Figure 4a. This shows that the bar has a relatively flat light profile with a sharp edge near deprojected radius $x_b = R_{\text{bar}} = 80''$ (vertical dotted line). The profile is typical of early-type barred galaxies (Elmegreen & Elmegreen 1985). The solid vertical line in Figure 4a shows a radius, $x_b = 58.5''$, where we will assume that the bar dominates the light profile, with little contribution from the bulge. The mean bar minor-axis profile at this radius, based on cuts from both sides of the nucleus and folded around the bar major axis, declines smoothly but reaches a plateau of $\mu_H = 19.55$ mag arcsec $^{-2}$, near $\pm 40''$, where it presumably blends with

TABLE 2
PHOTOMETRIC MODELS^a

Galaxy (1)	Filter (2)	Data Set (3)	Type of Fit (4)	μ_{01} (5)	σ or r_e (6)	μ_{02} (7)	σ or r_e (8)	μ_l (9)
NGC 1433.....	H	Bar minor axis	Double Gaussian	19.61	6.7	19.20	16.3	19.55
NGC 1433.....	H	Mean projected bulge	Double exponential	13.61	4.5	16.60	19.6	19.64
NGC 1433.....	H	Galaxy major axis, $r \leq 60''$	Double exponential	13.57	4.8	16.24	18.8	19.65
NGC 1433.....	B	$m = 0$ profile	Exponential	21.80	98.1
NGC 1433.....	I	$m = 0$ profile	Exponential	19.50	82.1
NGC 1433.....	H	$m = 0$ profile	Exponential	17.71	77.1
NGC 6300.....	H	Bar minor axis	Double Gaussian	19.70	7.0	18.93	11.3	18.35
NGC 6300.....	H	$m = 0$ profile	Exponential	16.77	67.8

^a Col. 1: Galaxy name; col. (2): filter; col. (3): profile fitted; col. (4): fitting function; col. (5): central surface brightness (mag arcsec $^{-2}$) of first (or only) component; col. (6): Gaussian width σ for Gaussian fit or effective radius for exponential fit of first (or only) component, in arcseconds; col. (7): central surface brightness (mag arcsec $^{-2}$) of second component; col. (8): Gaussian width or effective radius of second component, in arcseconds; Col. (9): lens surface brightness (mag arcsec $^{-2}$), if relevant.

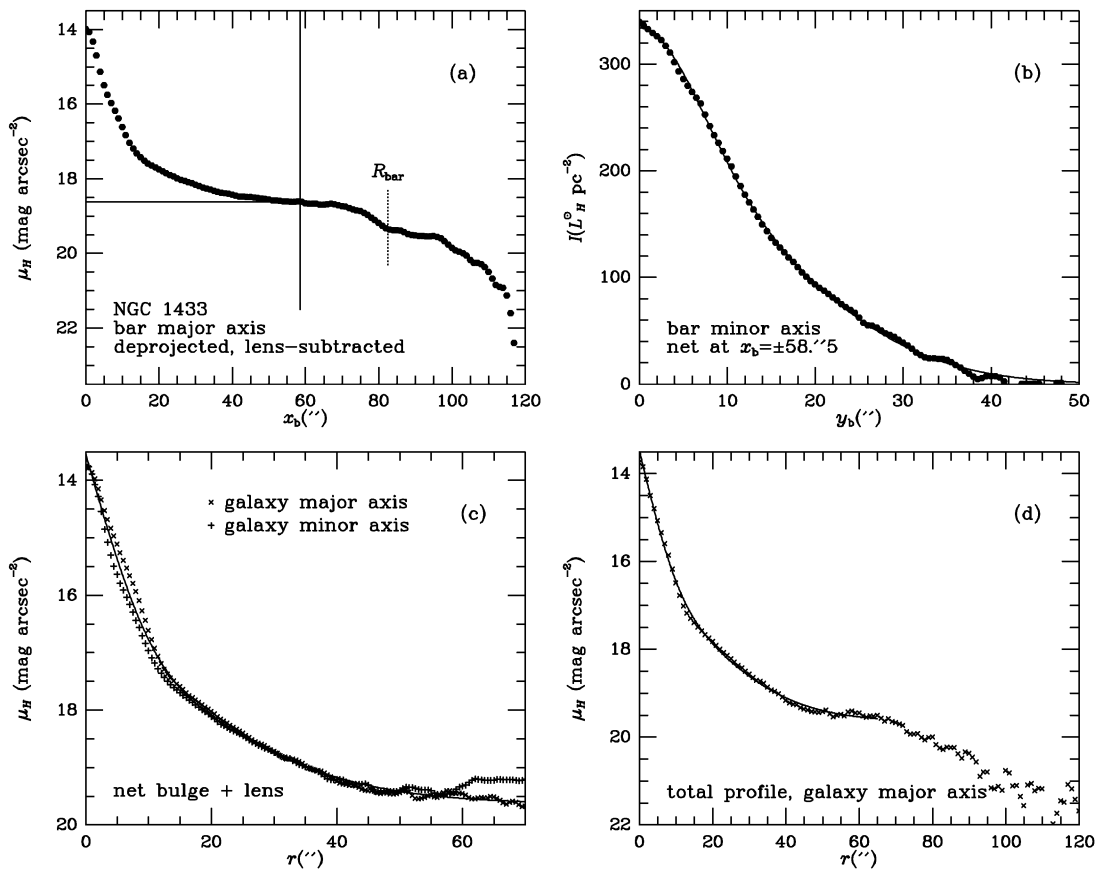


FIG. 4.—Photometric representations of the bar and bulge of NGC 1433 (see text). (a) Bar major-axis profile after subtraction of a constant lens surface brightness. The coordinate x_b is the radius along the deprojected bar axis, assuming an inclination of 33° and a line of nodes position angle of 201° . The vertical solid line refers to a reference radius, $x_b = 58''.5$, where the minor-axis profile of the bar was assumed to be uncontaminated by the bulge. The horizontal line shows the assumed surface brightness of the bar inside $58''.5$. The vertical dashed line shows the radius of the sharp end of the bar as seen on the H -band image, which we denote R_{bar} . (b) Net bar minor-axis profile after subtraction of a constant lens surface brightness and averaged around the bar and on both sides of the nucleus. The coordinate y_b is the distance along an axis perpendicular to the bar. The solid curve is a double Gaussian fit to the profile (see Table 2). (c) Profiles along the galaxy major and minor axes after removal of the primary bar as represented in (a) and (b). The radius r refers to distance from the center in the sky plane. The solid curve is a double exponential representation with a constant lens (see Table 2). (d) Surface brightness profile along the galaxy major axis with no components removed, to show that a double exponential plus lens representation still works for the central regions of the galaxy. The solid curve is a fit of such a representation (see Table 2).

the lens light distribution. We will therefore model the bar minor-axis light profile at $x_b = \pm 58''.5$ as the sum of the bar and a constant lens surface brightness of $\mu_H = 19.55$ mag arcsec $^{-2}$. Figure 4b shows the light profile perpendicular to the bar at this bar radius, after removal of the lens contribution. The net profile, in units of $L_H^\odot \text{pc}^{-2}$, is well represented by the sum of two Gaussian functions whose parameters are listed in Table 2.

With the double Gaussian representation, we then made a model of the H -band bar light distribution in two dimensions by assuming the bar has a constant surface brightness for $x_b \leq 58''.5$ (horizontal line, Fig. 4a) and a slightly declining surface brightness to its ends for $x_b > 58''.5$. In this representation, the primary bar exists throughout the central area and, within a circle of radius of $117''$, includes 15% of the total H -band luminosity. This model was reprojected and subtracted from the original image to reveal the projected structure of the bulge of NGC 1433. This bar-subtracted image is shown in Figure 5. The image shows that our bar representation successfully removes most of the primary bar, revealing a significant bulge that is rounder in its outer regions compared with its inner regions. Also, removal of the primary bar does not eliminate all of the

nonaxisymmetry, since the strong oval lens remains, as well as a secondary bar or oval inside the bulge.

Mean profiles of the net bulge plus lens light along the galaxy major and minor axes (average of position angles 21° and 201° and 111° and 291° , respectively) are shown in Figure 4c. The two profiles are different mainly inside $r = 10''$, where the small nuclear lens is found. Thus, the inner part of the bulge of NGC 1433 may be more triaxial than the outer part.

Evidence will be presented in § 4.5 that the inner part of the bulge of NGC 1433 is probably highly flattened compared with nonbarred galaxy bulges at the same absolute magnitude. If this is true also of the outer part, then the bulge would be elongated roughly along the bar axis in this region. The average of the major and minor-axis profiles in Figure 4c is well represented by the sum of two exponentials, after subtraction of a uniform lens component. The parameters of this representation are summarized in Table 2 (data set: mean projected bulge). Assuming a round shape in projection for the average profile, the two exponentials contribute 27% of the total H -band luminosity.

Note that the double exponential interpretation of the inner regions of NGC 1433 does not depend on our

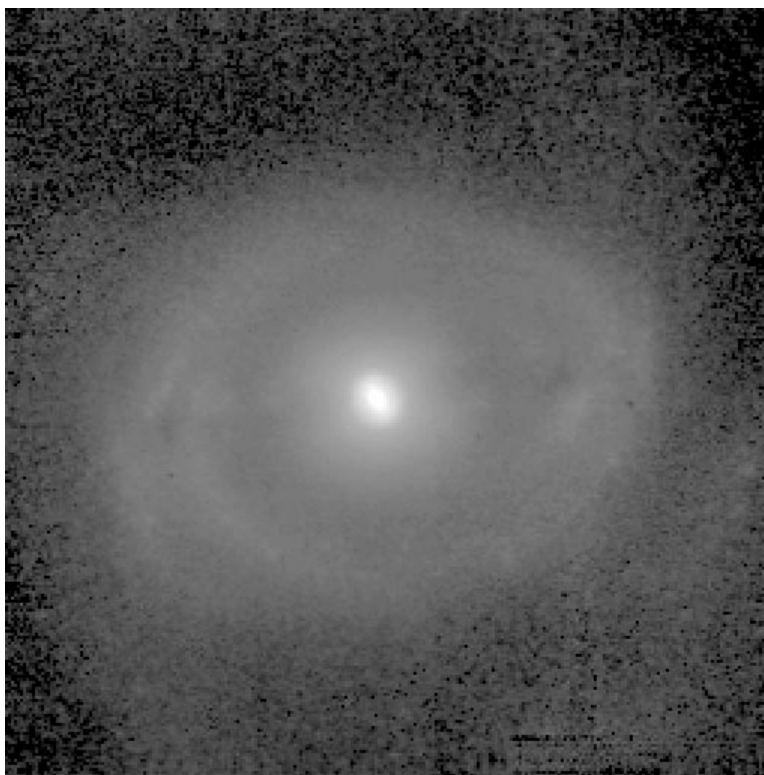


FIG. 5.—Sky plane H -band image of NGC 1433 with the primary bar (and all foreground stars) subtracted. The field shown is $4'.87$ square. Note the large round area surrounding the secondary lens and bar. North is at the top, and east to the left.

assumed bar model. Figure 4*d* shows a folded major-axis profile with the bar included. Along this axis to $r = 60''$, the profile can be represented as the sum of two exponentials plus a constant lens with the parameters listed in Table 2 (data set: galaxy major axis, $r \leq 60''$). This representation will be used for the asymmetric drift correction to stellar absorption line velocities in § 4.4.

4.3. Fabry-Perot Velocity Field and Rotation Curve

The sequence 1 RFP velocity field of NGC 1433 is shown in color code in Figure 6. This map is deeper and of higher precision than the contour velocity field published by B86, based on the TAURUS Fabry-Perot Interferometer, and includes H II regions in the outer spiral arms and plumes that were not covered by the TAURUS observations. As in B86, very little emission is found in the bar region, with only a few H II regions being detected. The nucleus, inner ring, and plumes are very well covered with emission, as already shown in H α maps presented by Crocker, Baugus, & Buta (1996) and Hameed & Devereux (1999). In contrast, emission in the outer pseudoring is much fainter than in these other features and as a consequence the optical rotation curve cannot be determined very reliably in the outer regions of the galaxy. Fortunately, we have the H I rotation curve for this region. As in B86, the line of nodes appears to be nearly along the projected minor axis of the inner ring, implying that this feature is intrinsically elongated along the bar axis.

The dynamical parameters of NGC 1433 were derived using the iterative method of Warner, Wright, & Baldwin (1973). Although the basic assumption in this method is that only circular motions are present, we can still derive an

approximate rotation curve that can be compared with the H I rotation curve. Our two RFP velocity fields were analyzed separately, and all velocity points were used for the iterations. Since the inclination cannot be reliably derived from such a sparse velocity field viewed at low inclination, this parameter was fixed to the photometric value of 33° for all iterations. For both RFP velocity fields, the rotation center was found not to be significantly different from the red continuum center, and the receding line of nodes position angle was found to be $199^\circ \pm 1^\circ$. The systemic velocity was measured to be $1074 \pm 2 \text{ km s}^{-1}$. These parameters are in very good agreement with those derived by B86 and by Ryder et al. (1996). For the purposes of all of our further analysis, however, we will adopt the H I position angle of 201° since it is based on a more complete velocity field that includes the outer pseudoring, whereas the RFP position angle is based mainly on the inner ring and plumes.

Figure 7 shows the rotation curves derived from both RFP sequences at $30''$ resolution, to effect a legitimate comparison between the H α and H I rotation curves. Between $45''$ and $135''$, the RFP velocities are slightly higher than the H I velocities by about 11 km s^{-1} , while at larger radii the difference is about -13 km s^{-1} . The two H α sequences agree well with each other, but they are not independent since both used the same calibration and were obtained on the same night with the same setup. The agreement between the H α and H I rotation curves is reasonable, considering the sparse coverage of the optical velocity field.

Table 3 lists the combined sequence 1 and 2 data at different resolutions for the inner and outer regions (see Fig. 8). For $r \leq 15''$, the resolution is $2''$, while at $47.5''$ it is $5''$, and at larger radii it is $10''$ and $20''$. In the inner regions, the H α

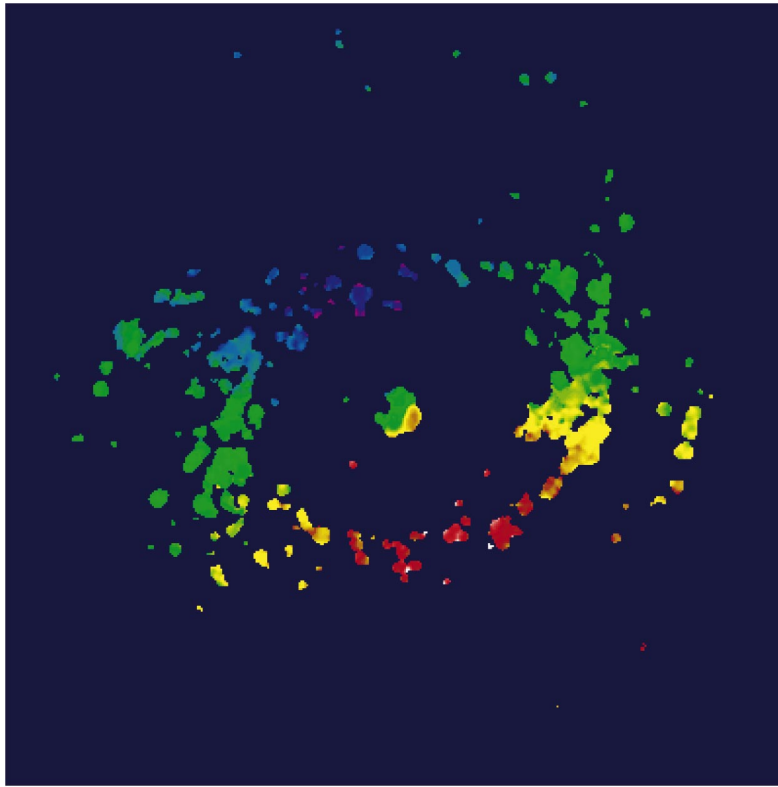


FIG. 6.—Fabry-Perot velocity field of NGC 1433. The color code is such that red corresponds to about 1170 km s^{-1} and blue corresponds to about 980 km s^{-1} . The field of view is 6.38 square, with north to the top and east to the left.

rotation curve appears to rise approximately linearly with increasing radius as $V_c(r) = 9.01r$ in a solution where the line is forced to pass through the origin (*dashed line*, Fig. 8).

4.4. Stellar Rotation Velocities and Velocity Dispersions

The raw velocities and velocity dispersions from the Fourier quotient method (STSDAS routine FQUOT) are shown in Figure 9. Along position angle 17° , we see a rotation profile rising to an apparent maximum of 57 km s^{-1} at a radius of $6''$. The location of this maximum actually correlates with structure in the galaxy. In the H -band image, the nuclear ring of NGC 1433 takes on the appearance of a

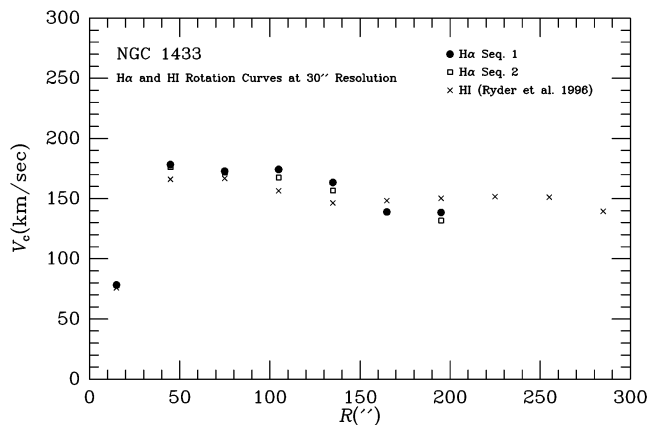


FIG. 7.—Comparison between $H\alpha$ Fabry-Perot and $H\text{ I}$ rotation curves for NGC 1433, at similar resolution.

TABLE 3
 $H\alpha$ FABRY-PEROT ROTATION VELOCITIES IN NGC 1433^a

R (arcsec) (1)	$e(R)$ (arcsec) (2)	V_c (km s^{-1}) (3)	$e(V_c)$ (km s^{-1}) (4)
1.0	1.0	16.7	8.7
3.0	1.0	31.6	5.0
5.0	1.0	44.0	4.1
7.0	1.0	66.8	4.2
9.0	1.0	90.4	4.0
11.0	1.0	100.0	2.9
13.0	1.0	108.4	2.9
15.0	1.0	133.5	4.9
47.5	2.5	175.5	13.1
55.0	5.0	177.5	0.4
65.0	5.0	172.6	1.7
75.0	5.0	173.7	0.4
85.0	5.0	171.0	0.2
95.0	5.0	172.5	2.2
110.0	10.0	157.8	12.7
130.0	10.0	159.7	2.9
150.0	10.0	156.4	8.0
170.0	10.0	141.9	3.1
190.0	10.0	133.9	4.5
210.0	10.0	155.1	10.2

^a Col. (1): radius along major axis; col. (2): radius range half-width; col. (3): mean rotation velocity; col. (4): internal error in mean rotation velocity.

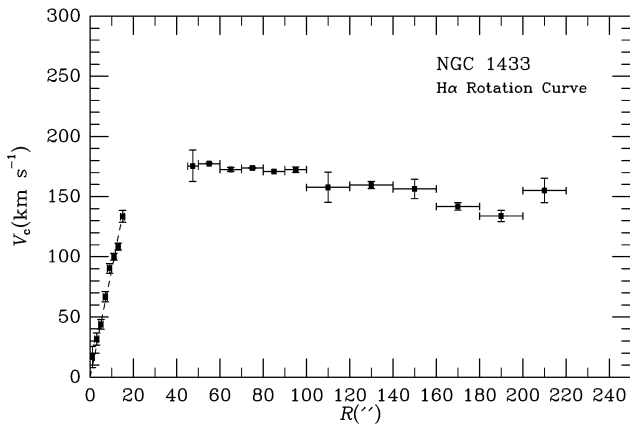


FIG. 8.—Mean H α rotation curve of NGC 1433, with 2'' resolution in the inner regions and 5''–20'' in the outer regions.

shallow brightness profile, more like a lens than a ring. From ellipse fits to this region, the radius of the ellipse having maximum ellipticity along the position angle of 17° is shown as the vertical dashed line in Figure 9c. This radius

corresponds exactly to the turnover point in the rotation profile. The radius of this same ellipse along position angle 96° is shown in Figure 9d. Along both position angles, there is a slight drop in velocity dispersion just beyond these radii, but its significance is only 1–2 σ . Only a small amount of rotation is detected along position angle 96°, which is displaced only 15° from the galaxy minor axis.

The cross-correlation method (Tonry & Davis 1979, included as routine XCOR in STSDAS) was also used to derive a rotation profile along position angle 17°. We found this routine to be more stable than FQUOT in deriving rotation velocities at larger radii, and we were able to determine rotation velocities to $r = 65''$ along this position angle. The XCOR rotation profile corrected for an inclination of 33° and for the 4° offset from the adopted line of nodes is listed in Table 4.

Even after correction for orientation, the maximum stellar rotation velocity at turnover (inside $R = 10''$) is only 60% of the velocity reached in the range 45''–70'', where the maximum in the gas velocities occurs. It is likely that some of this difference is simply due to pressure support owing to the relatively high velocity dispersion in the inner regions. Following van der Kruit & Freeman (1986 and references therein), we estimate the asymmetric drift in the inner

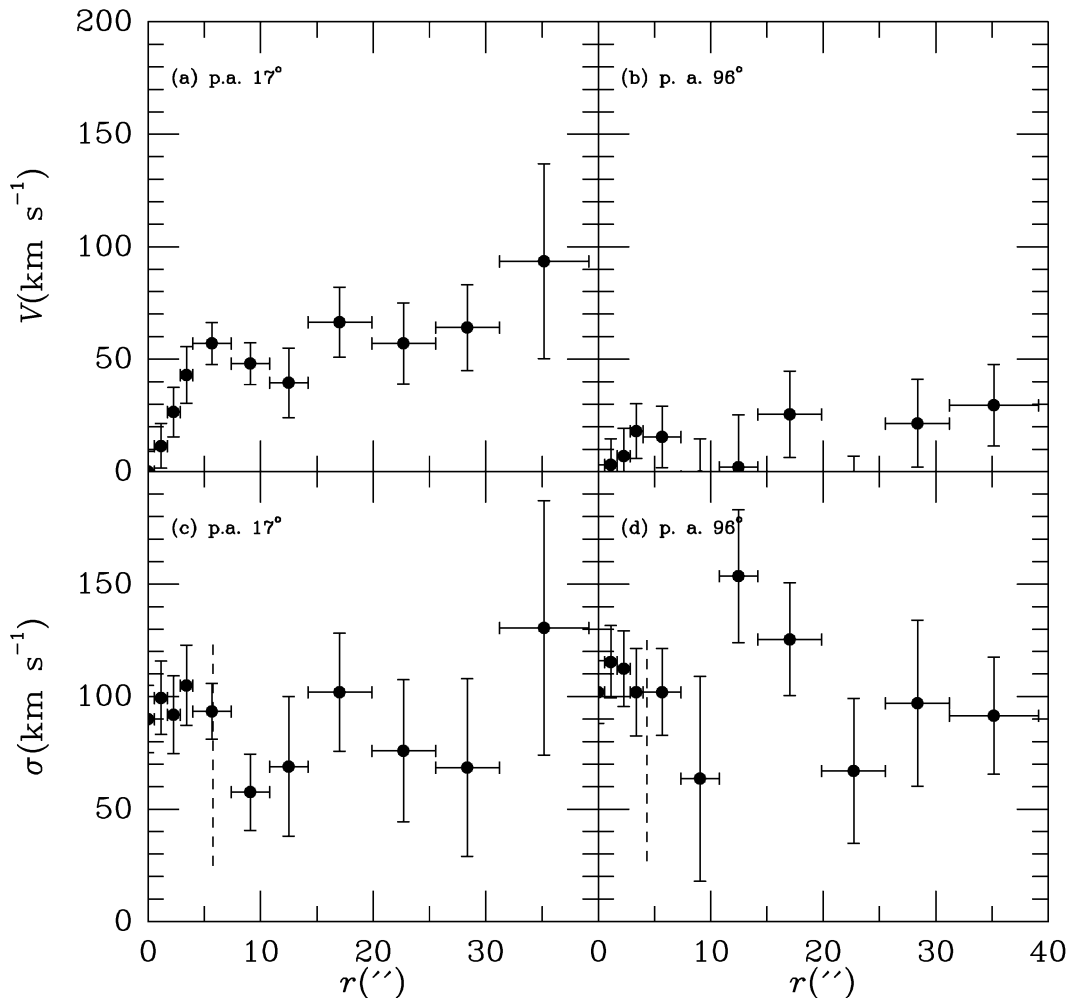


FIG. 9.—Rotation velocities and velocity dispersions along position angles 17° (photometric major axis) and 96° (bar major axis), based on long-slit spectra and analyzed using the Fourier quotient technique. The vertical dashed lines show where the isophote of maximum ellipticity in the bulge is crossed along each position angle.

TABLE 4
STELLAR ROTATION VELOCITIES IN NGC 1433^a

R (arcsec)	$e(R)$ (arcsec)	V_* (km s ⁻¹)	$e(V_*)$ (km s ⁻¹)	V_c (km s ⁻¹)
(1)	(2)	(3)	(4)	(5)
0.0	0.6	3.7	10.1	...
1.1	0.6	24.0	12.0	...
2.3	0.6	53.4	15.8	76.6
3.4	0.6	79.2	15.7	115.2
4.5	0.6	93.0	14.3	138.0
5.7	0.6	100.0	11.1	152.1
6.8	0.6	110.5	13.4	165.8
8.0	0.6	99.0	12.9	162.8
9.1	0.6	101.8	12.4	166.9
11.4	1.7	88.4	14.3	159.3
14.8	1.7	99.5	17.1	160.6
18.2	1.7	103.6	22.0	158.5
21.6	1.7	103.6	19.9	156.3
26.1	2.8	111.9	17.2	160.7
37.5	8.5	138.5	20.5	175.4
57.9	11.9	164.6	18.1	184.2

^a Col. (1): radius along major axis; col. (2): spectral aperture half-width; col. (3): mean stellar rotation velocity; col. (4): error in mean stellar rotation velocity; col. (5): true circular velocity, after approximate correction for asymmetric drift.

regions of NGC 1433 using the following expression:

$$V_c^2 - V_*^2 = -\sigma_R^2 \left[\frac{\partial \ln v}{\partial \ln R} + \frac{\partial \ln \sigma_R^2}{\partial \ln R} + \left(1 - \frac{\sigma_\phi^2}{\sigma_R^2} \right) + R \sigma_{Rz}^2 \frac{\partial (\ln v \sigma_{Rz}^2)}{\partial z} \right], \quad (1)$$

where V_* is the observed mean stellar rotation velocity, V_c is the true circular velocity, v is the stellar volume density, and σ_R , σ_ϕ , and σ_z are the radial, tangential, and vertical components, respectively, of the velocity ellipsoid. We note equation (1) is strictly valid only in the case of axisymmetry and that estimating its various terms involves several assumptions. The first term involving the stellar density is usually derived by assuming the galaxy is well approximated by an isothermal sheet, so that the three-dimensional light distribution of the old disk population varies as $e^{-R/h} \text{sech}^2(z/z_o)$, where h and z_o are radial and vertical scale lengths. If the mass-to-light ratio is constant and z_o is independent of R , then the surface brightness distribution can be used to estimate $\partial \ln v / \partial \ln R$. We have shown (Fig. 4d) that along the major axis the surface brightness distribution in NGC 1433 can be approximated as the sum of two exponentials and a constant lens brightness:

$$I = I_{01} e^{-(R/h_1)} + I_{02} e^{-(R/h_2)} + I_\ell. \quad (2)$$

This is a more complicated profile and may not be strictly related to the actual stellar volume density. However, the volume density from each individual exponential component will probably scale with the surface brightness, so that we can still approximate $\partial \ln v / \partial \ln R$ with $\partial \ln I / \partial \ln R$.

The second term in equation (1) involves the derivative of the radial velocity dispersion, σ_R , while we have measured velocity dispersions along two position angles, neither of which coincides exactly with the major or the minor axis. To derive σ_R along the major axis of the galaxy, we need to make assumptions about the intrinsic velocity dispersion anisotropy in the galaxy. Figure 10 shows that there might

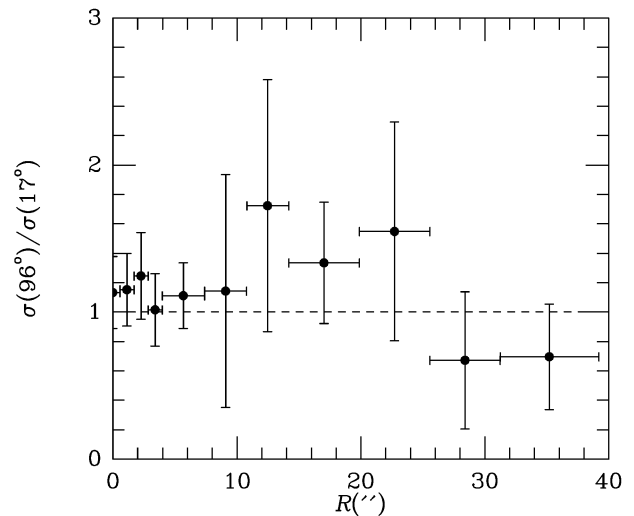


FIG. 10.—Ratio of velocity dispersion along position angle 96° to that along position angle 17° vs. radius in the galaxy plane.

be some slight velocity dispersion anisotropy in the inner regions of NGC 1433. It shows $\sigma(96^\circ)/\sigma(17^\circ)$ as a function of radius. Although most of the points are higher than 1.0, none is significantly different from 1.0. However, to examine this further, we need to allow for the contribution of the instrumental velocity dispersion, σ_i , to our measured dispersions. According to Kormendy & Illingworth (1983), the Fourier quotient method gives a velocity dispersion approaching σ_i as $\sigma_{\text{true}} \rightarrow 0$. Our instrumental velocity dispersion is 47 km s^{-1} , based on analysis of comparison arc emission lines, which are assumed to have very small intrinsic widths. Restricting to radii between 1" and 7" along both 17° and 96°, and after removing σ_i in quadrature from the observed dispersions, we estimate $\sigma_c(96^\circ)/\sigma_c(17^\circ) = 1.16 \pm 0.17$. This ratio is an approximation to σ_R/σ_ϕ diluted by σ_z . We find (in the plane parallel approximation) that the assumption $\sigma_\phi = \sigma_z = \sigma_R/\sqrt{2}$ would give a predicted ratio of 1.08 for the same position angles. We refer to this as case 1, and, assuming this relation between the velocity dispersion components, we infer from the major-axis dispersions the σ_R versus R relation shown in Figure 11. The solid line shows a weighted least-squares fit to the points described by

$$\sigma_R = 112.5 - 1.036R. \quad (3)$$

No more complicated function is justified, and we use this formula in equation (1). However, disks which are locally isothermal and of constant M/L , which have a vertical scale height independent of radius, and which follow an exponential decline in surface brightness with radius are expected to have a dispersion that declines as $e^{-(R/2h_R)}$, where h_R is the radial scale length (Bottema 1993). As discussed in § 4.2, we cannot characterize the light distribution in the inner regions of NGC 1433 in terms of a single radial scale length.

Note that with our assumption that $\sigma_\phi = \sigma_R/\sqrt{2}$, the third term in equation (1) becomes a constant, 0.5. At $R = 7''$, the first term in equation (1) (using photometric H -band model “galaxy major axis, $r \leq 60''$ ” from Table 2) is -1.7 while the second term, based on equation (3), is -0.13 , so that the first term is the dominant term. This remains the case to $R = 40''$. The last term in equation (1) is discussed by van der Kruit & Freeman (1986). For a self-gravitating sheet, or a flat rotation curve, the term is 0,

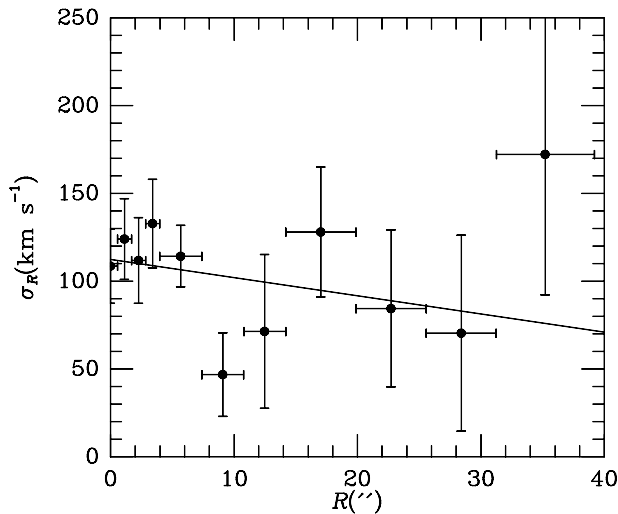


FIG. 11.—Plot of radial velocity dispersion σ_R vs. radius R in the galaxy plane. The plot assumes the relationship between the velocity dispersion components is $\sigma_\phi = \sigma_z = \sigma_R/\sqrt{2}$. The solid line represents equation (3).

while if the velocity ellipsoid everywhere points toward the galaxy center, then the term becomes $1 - \sigma_z^2/\sigma_R^2$. We will assume the plane parallel approximation is everywhere valid for NGC 1433, so that this term vanishes. Ignoring this term is probably most justified outside the rotation curve maximum, where the rotation velocities are nearly constant.

We have investigated other assumptions concerning the velocity dispersion components. If the velocity dispersion tensor is isotropic (case 2), which is not ruled out by our data, then the mean value of V_c over the range $6''.8 \leq R \leq 26''$ is 144 km s^{-1} , compared with 161 km s^{-1} for case 1 over the same radius range. On the other hand, old Galactic disk dwarfs and giants have dispersion components in the approximate relation $\sigma_R = \sqrt{2}\sigma_\phi = 2\sigma_z$ (Mihalas & Binney 1981). This is also not ruled out by our data since the low inclination means we mostly see σ_z . If this kind of relation holds in NGC 1433 (case 3), then $\langle V_c \rangle$ over the above radius range is 192 km s^{-1} . We note that from the Tully-Fisher relation, the maximum in the rotation curve is not likely to be higher than our case 1 assumptions predict, so that our analysis probably brackets the true inner rotation curve in NGC 1433. If we set the maximum rotation velocity to 160 km s^{-1} , then using equations (1), (5), and (9) of Tully et al. (1998) and our value of $I_T = 8.90$, we estimate a distance of 12.1 Mpc, comparable to the distance listed by Tully (1988) and based on the radial velocity.

Figure 12 compares the H α and stellar rotation curves of NGC 1433. The filled circles in this figure (see also Table 4) show the corrected stellar rotation velocities with the case 1 assumptions used for the asymmetric drift. In spite of the uncertainties, the rotation curve maximum is about the same level as given by the gas velocities beyond $R = 50''$, and the stellar rotation curve connects smoothly with the gas velocities at these radii. Also, the stellar rotation curve rises much more steeply than the gaseous rotation curve inside $r = 20''$. This could be due in part to noncircular motions, but it could also be due to the fact that the gas in the central area may be less concentrated than the stars, and therefore velocities, being also weighted by density, have a lower gradient for the gas. Since there is a strong twist in the

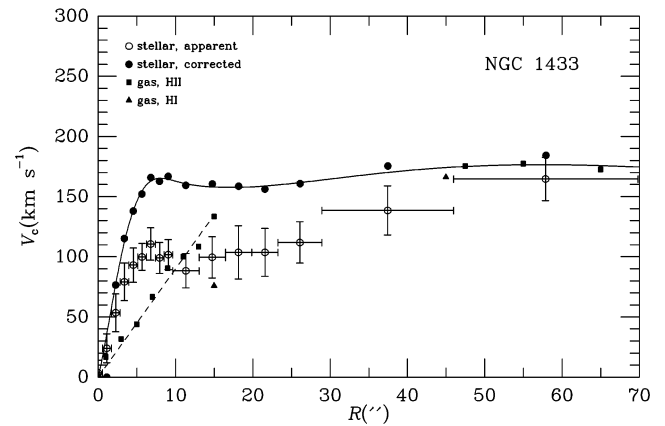


FIG. 12.—Inner rotation curve of NGC 1433, based on stellar absorption lines, H α Fabry-Perot interferometry, and H I. The solid curve is a polynomial representation of the combined stellar/gaseous rotation curve corrected for asymmetric drift (see text).

isovelocity contours in Figure 6, noncircular motions are likely to be important in this region.

The solid curve in Figure 12 is simply a representation of the corrected velocities and is based on fits of a polynomial to various ranges in radius. This polynomial is useful for computing precession frequencies in NGC 1433. Figure 13 shows our final composite rotation curve based on both stellar and gaseous velocities with a full polynomial representation, while Figure 14 shows the angular velocity Ω and precession frequencies $\Omega \pm \kappa/2$ and $\Omega \pm \kappa/4$, where κ is the radial epicyclic frequency, as a function of radius. The inner and outer radius of each ring from Table 1 is indicated in Figure 14, where “nr” stands for nuclear ring, “r” for inner ring, and “R” for the outer pseudoring. The plot also indicates the inner and outer radii of the plume features, which arc over a mean radius range of 7.2 to 10.2 kpc, and the radius of the sharp ends of the bar. Buta & Combes (2000) show that numerical simulations favor a pattern speed of

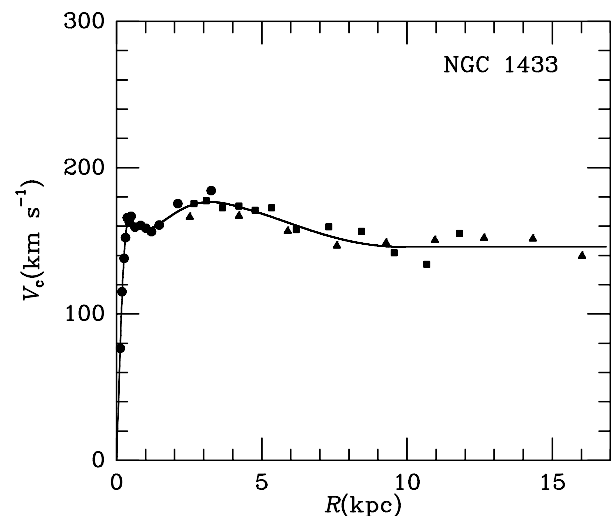


FIG. 13.—Composite rotation curve of NGC 1433. Filled circles refer to stellar absorption line velocities corrected approximately for asymmetric drift, filled squares refer to average velocities from the sequence 1 and 2 Fabry-Perot velocity fields, and filled triangles show the H I velocities. The solid curve is a polynomial representation derived by trial and error. The radius scale is based on a distance of 11.6 Mpc.

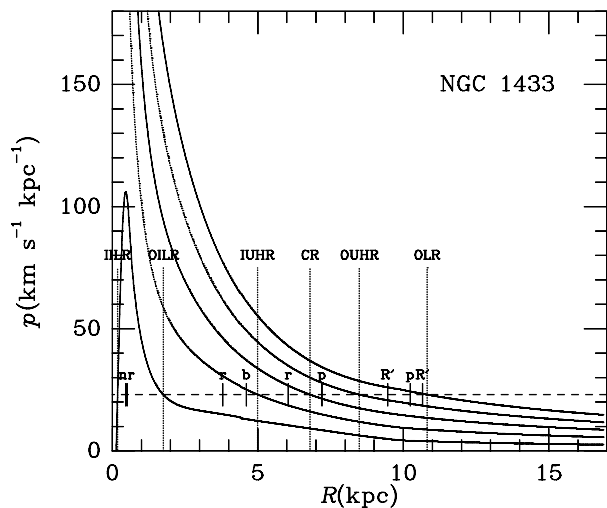


FIG. 14.—Lindblad precession frequencies in NGC 1433, based on the polynomial representation of the rotation curve shown in Fig. 13. The curves from left to right are: $\Omega - \kappa/2$, $\Omega - \kappa/4$, Ω , $\Omega + \kappa/4$, and $\Omega + \kappa/2$, where Ω is the circular angular velocity and κ is the epicyclic frequency. The deprojected locations of all of the main features of the galaxy are indicated: “nr” = nuclear ring; “r” = inner ring; “b” = bar; “p” = plumes; and “R” = outer pseudoring. For the rings and plumes, both major- and minor-axis radii are indicated. The plot also indicates the locations of all of the major resonances in the galaxy for a pattern speed of $23 \text{ km s}^{-1} \text{ kpc}^{-1}$ (horizontal dashed line).

$\Omega_p = 23 \text{ km s}^{-1} \text{ kpc}^{-1}$. For this pattern speed (horizontal dashed line, Fig. 14), we get the resonance locations listed in Table 5. The outer pseudoring lies close to and slightly inside the outer Lindblad resonance (OLR), where $\Omega_p = \Omega + \kappa/2$, the inner pseudoring straddles the inner 4:1 resonance (IUHR), where $\Omega_p = \Omega - \kappa/4$, while the nuclear ring lies between two inner Lindblad resonances (ILRs), where $\Omega_p = \Omega - \kappa/2$. Perhaps the most interesting findings from this plot are how the plumes straddle the outer 4:1 resonance (OUHR), where $\Omega_p = \Omega + \kappa/4$, and how the predicted location of corotation (CR), where $\Omega_p = \Omega$, lies between the *maximum* radius of the inner ring and the *minimum* radius of the plumes. In contrast, the maximum radius of the plumes comes close to OLR.

The plot also shows that the sharp ends of the primary bar of NGC 1433 lie far inside CR, and in fact just inside the IUHR. We estimate a ratio $R_{\text{CR}}/R_{\text{bar}}$ of 1.5. Thus, the transition from bar to spiral arms (in the inner pseudoring) occurs between IUHR and CR in NGC 1433, for the adopted pattern speed. This is fairly typical, as discussed by Elmegreen (1996), who argues that higher order resonances between IUHR and CR crowd to terminate bars well before CR is reached.

TABLE 5
RESONANCE LOCATIONS IN NGC 1433 FROM POLYNOMIAL
ROTATION CURVE^a

Resonance	Radius (kpc)
Inner inner Lindblad resonance (ILR)	0.2
Outer inner Lindblad resonance (OILR)	1.7
Inner 4:1 ultraharmonic resonance (IUHR)	5.0
Corotation (CR)	6.8
Outer 4:1 ultraharmonic resonance (OUHR)	8.5
Outer Lindblad resonance (OLR)	10.8

^a For a fixed pattern speed of $\Omega_p = 23 \text{ km s}^{-1} \text{ kpc}^{-1}$.

Ryder et al. (1996) also made a pattern speed estimate and derived precession frequency curves for NGC 1433, based on the H I rotation curve alone. Assuming that the outer pseudoring lies at OLR, they derived $\Omega_p = 26 \pm 5 \text{ km s}^{-1} \text{ kpc}^{-1}$.

4.5. Ordered versus Random Motions in NGC 1433

As noted by Kormendy (1982 and references therein), the ratio of maximum observed rotation velocity V_{max} to the mean velocity dispersion $\langle \sigma \rangle$ is a measure of the relative importance of rotation and random motion in a stellar system. For NGC 1433, V_{max} (in the bulge region, $R < 10''$) is $103 \pm 7 \text{ km s}^{-1}$ (Table 4), while the mean velocity dispersion (corrected for instrumental dispersion) along position angle 17° in the range $1'' \leq R \leq 7''$ (just outside the nucleus) is $\langle \sigma_c \rangle = 84 \pm 9 \text{ km s}^{-1}$. These give a ratio $V_{\text{max}}/\langle \sigma_c \rangle = 1.22 \pm 0.15$. The maximum apparent ellipticity achieved in the bulge region of NGC 1433 is $\epsilon = 0.31$, based on our *H*-band image. For this bulge ellipticity, $V_{\text{max}}/\langle \sigma_c \rangle$ is 1.8 times that predicted for an oblate bulge model flattened solely by rotation (see Illingworth 1981). Kormendy (1982) showed that such high ratios are typical of triaxial bulges in SB galaxies, and suggested that such bulges rotate more rapidly and are more highly flattened than SA bulges. Kormendy (1993) argues that the features we see to be bulges in many SB galaxies are largely disk light. Kormendy’s conclusion was based mainly on SB0 galaxies, but it apparently applies also to early type SB spirals as well. Further evidence for a highly flattened bulge in NGC 1433 is provided by the correlation between central velocity dispersion and absolute bulge magnitude for disk galaxies (Kormendy & Illingworth 1983). SA bulges follow a fairly well-defined relation for these parameters, while SB bulges tend to have lower central velocity dispersions for a given bulge absolute magnitude. Our *H*-band bulge model in § 4.2 contains 27% of the total luminosity of NGC 1433. If we assume this is also true in *B*, then the absolute blue magnitude of the bulge is low, $M_B \geq -18.4$. NGC 1433’s central velocity dispersion is $84 \pm 7 \text{ km s}^{-1}$, which is very low (by almost a factor of 2) compared with an SA bulge of the same M_B (see Fig. 1 of Kormendy & Illingworth 1983, after adjustment for distance scale).

5. ANALYSIS OF NGC 6300

5.1. Morphology and Surface Photometry

Our *H*-band image of NGC 6300 is shown in Figure 15. This shows that the bar and inner pseudoring are very strong in the near-IR. One of the first tests we can make with this image is the location of the nucleus. B87 found that radial velocity profiles near the major axis of NGC 6300 were not symmetric with respect to the apparent nucleus on slit spectra taken near H α . B87 suggested this discrepancy was due to internal extinction, which is shown prominently in a *U*-band image as a dust lane crossing near the center (see Fig. 3 of B87). To evaluate the extinction idea, we used IRAF routines GEOMAP and GEOTRAN to accurately transform our RFP red continuum image to the exact same coordinate system as our *H*-band image. There are many foreground stars toward NGC 6300 that makes this transformation reliable. The result gave an *H*-band nucleus displaced only $0^{\circ}02$ east and $0^{\circ}40$ south of the red continuum nucleus, far less than the $5''$ offset B87 deduced from a rotation curve analysis. The smaller offset is

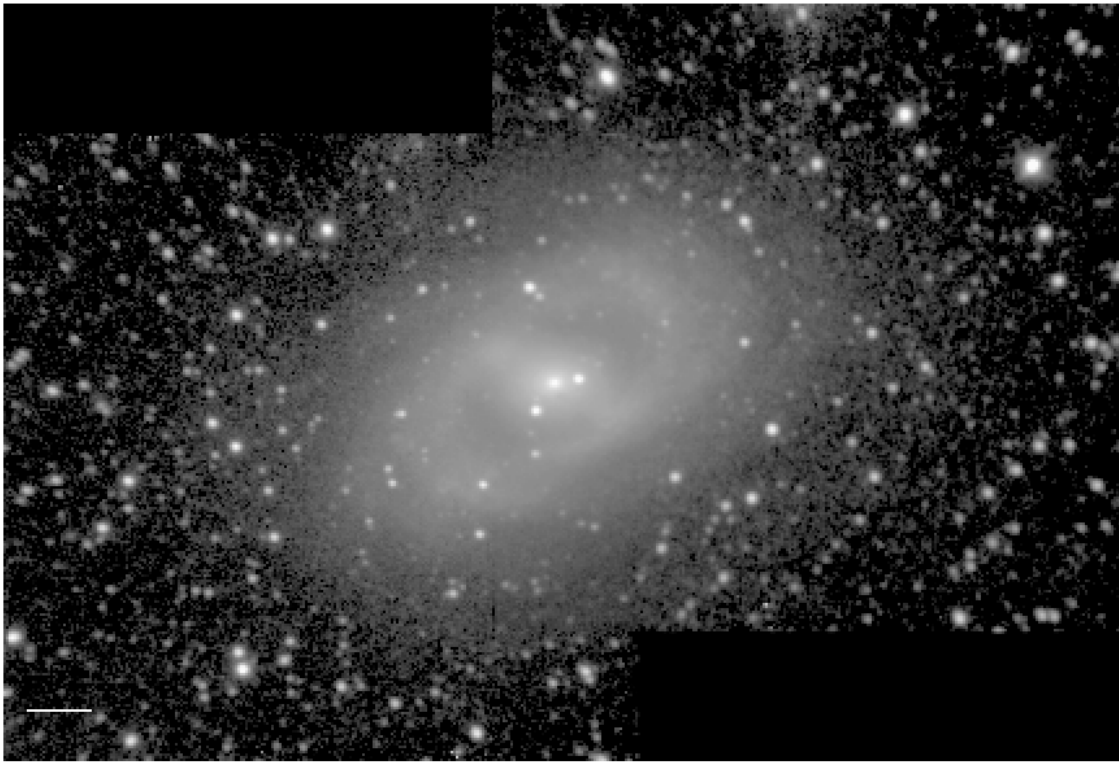


FIG. 15.—*H*-band mosaic image of NGC 6300, based on two offset fields. The field of view of the mosaic is 8.2×5.5 . The image is in units of mag arcsec^{-2} over the range 14.0–24.0 mag arcsec^{-2} . The scale bar in the lower left of the image is 2 kpc in length. North is at the top, and east to the left.

consistent with *HST* NICMOS observations of the nucleus presented by Regan & Mulchaey (1999), who found the peak of dust emission is displaced slightly south of the nucleus. An *HST* wide *V* filter image of NGC 6300 (Malkan, Gorjian, & Tam 1998) confirms that most of the extinction near the center of NGC 6300 is to the south and west of the apparent nucleus, not to the east. Extinction is therefore *not* the cause of the rotation center offset.

We were not able to derive a reliable zero point for our *H*-band image since the observations were taken through some cirrus clouds. Instead, we have bootstrapped a zero point by comparing our *H*-band photometry with a published ellipse-fit profile in the *K*-short (or *K_s*) passband, at $2.1\mu\text{m}$ from Mulchaey, Regan, & Kundu (1997). Using software from the IRAF package ISOPHOTE, we computed an *H*-band ellipse-fit profile and compared it with that of these authors. In the radius range $42'' \leq a \leq 60''$, both profiles are nearly constant, and from a comparison in this range we deduced a zero point assuming a typical value of 0.25 for $H - K_s$. With our inferred zero point, we derived the azimuthally averaged surface brightness profile shown in Figure 16. This profile was computed at the same radii and uses the same averaging ellipse used by B87: a position angle of 108° and an axis ratio of 0.64. The profile is very similar to that derived by B87 in *B* and *V*, and the bottom panel of Figure 16 shows the inferred azimuthally averaged color index profile. The color gradient in NGC 6300 is confined mainly within the inner pseudoring. From our azimuthally averaged profile, we deduce a total magnitude of $H_T = 7.0 \pm 0.2$ for NGC 6300, by extrapolating the surface brightnesses for $r > 180''$ as an exponential. The uncertainty is mainly in the zero point and not in the extrapolation of the profile. We also fitted an exponential to the slope under-

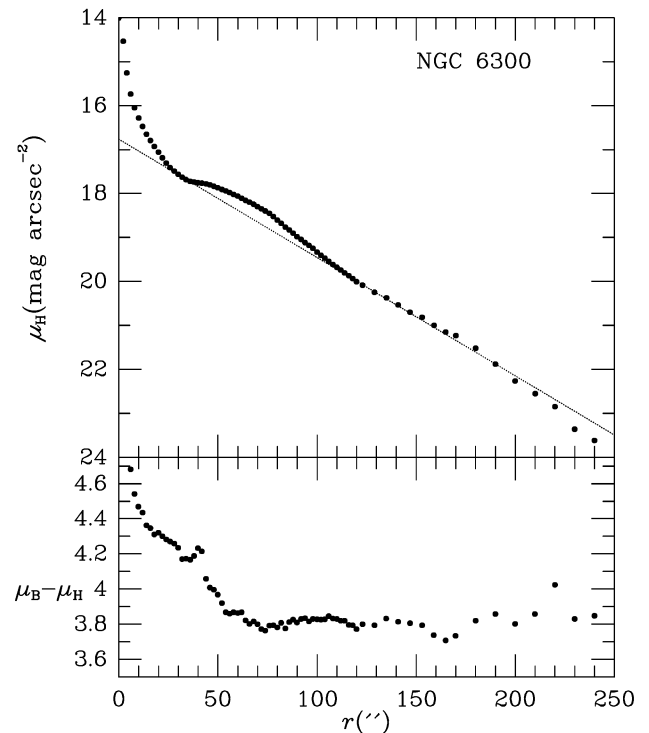


FIG. 16.—Azimuthally averaged *H*-band surface brightness profile of NGC 6300, based on the orientation parameters derived by B87 (ellipse axis ratio 0.64, ellipse position angle 108°). The color index profile is based on B87's *B*-band profile from photographic surface photometry. The dotted line represents an exponential fit to the background underlying the inner ring hump (see Table 2).

lying the inner ring hump (*dotted line*, Fig. 16). The parameters of this fit are summarized in Table 2.

In the left panel of Figure 17, we show our H -band image of NGC 6300 after deprojection, assuming an inclination of 52° and a line of nodes of 108° . In this image the bar has been rotated to the horizontal position. This reveals once again what was first noted by B87: that the inner pseudoring of NGC 6300 is not aligned along the bar axis, as is the inner pseudoring of NGC 1433. The misalignment amounts to about 80° . This is very atypical of SB inner rings and pseudorings (Buta 1995), but other examples are known (see Fig. 32 of Buta 1995 and Buta, Purcell, & Crocker 1995). In the right panel of Figure 17, we show the deprojected image after subtraction of the $m = 0$ Fourier component. This reveals a clear four-armed spiral structure in the inner regions, with two arms forming most of the inner pseudoring and two others lying just outside the major axis of the ring.

5.2. Bar and Bulge Properties

The bar and bulge in NGC 6300 were analyzed in a manner similar to NGC 1433. The H -band image was deprojected as before, with the line of nodes in the horizontal position. In this image, the bar has a position angle of 30.2° . To define the bar minor-axis profile, perpendicular cuts were taken across the bar at deprojected bar radii $x_b = \pm 34''$, where it was assumed that the bulge contributed little if any light. This position is shown in Figure 18a. The two cuts perpendicular to the bar were found not to agree well with each other or around the bar axis. The net bar minor-axis profile in Figure 18b is based on a sloped “lens” background, which was subtracted off. As for NGC 1433, we found that a double Gaussian can represent the bar minor-axis profile of NGC 6300, although the representation is poorer than for NGC 1433. The parameters of the two Gaussians are listed in Table 2.

As for NGC 1433, the bar of NGC 6300 is assumed to cross the center with a uniform surface brightness for $x_b \leq 34''$ (*horizontal line*, Fig. 18a). With this assumption, a model of the bar in two dimensions was made. This model was deprojected and subtracted from the original image, giving

TABLE 6
BULGE PROFILE FOR NGC 6300 FROM KENT (1986) METHOD

R (arcsec)	μ_H (mag arcsec $^{-2}$)	R (arcsec)	μ_H (mag arcsec $^{-2}$)
0.00.....	14.09	8.02	17.33
0.50.....	14.08	8.64	17.48
1.00.....	14.22	9.26	17.63
1.24.....	14.33	9.88	17.76
1.85.....	14.54	10.49	17.89
2.47.....	14.86	11.11	18.01
3.09.....	15.21	11.73	18.13
3.70.....	15.51	12.35	18.25
4.32.....	15.84	12.96	18.36
4.94.....	16.15	13.58	18.46
5.56.....	16.45	14.20	18.57
6.17.....	16.67	14.81	18.67
6.79.....	16.98	15.43	18.76
7.41.....	17.17

the net image in Figure 19. This reveals the probable bulge light as a somewhat flattened subsystem. Isophote shapes in this region have an apparent axis ratio of 0.81 in the inner regions but decrease to 0.64 in the outer regions, the same as the outer disk light measured by B87. Also, the outer parts of the apparent bulge have a major-axis position angle almost identical with that of the outer disk. Some of this apparent bulge light is therefore probably as flattened as the disk. With the bar removed, we computed profiles along the galaxy major and minor axes in order to use the method of Kent (1986) to derive the bulge profile. Figure 18c shows these profiles as well as the derived bulge profile (see Table 6). The Kent method can only extract the part of the bulge profile that is less flattened than the disk. For the decomposition, we used a disk flattening of $1/0.640$ from B87 and a bulge flattening of $1/0.81$. The method did not give reliable results beyond $r = 15''$, and the dashed curve in Figure 4c shows an extrapolation of an $r^{1/4}$ law fit to the surface brightnesses for $6.8 \leq r \leq 15.0$. With this representation, the bulge of NGC 6300 is found to contain 9.3% of the total

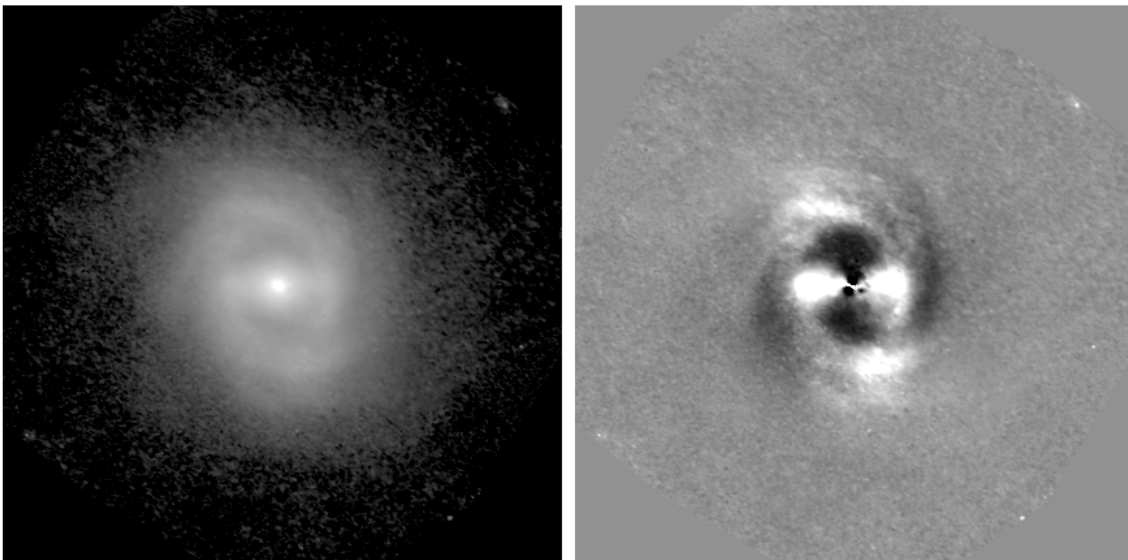


FIG. 17.—*Left*: deprojected H -band image of NGC 6300 based on an inclination of 52° and a line of nodes position angle of 108° , from B87. *Right*: the same image after subtraction of the $m = 0$ Fourier component. The bar axis has been rotated to the horizontal position.

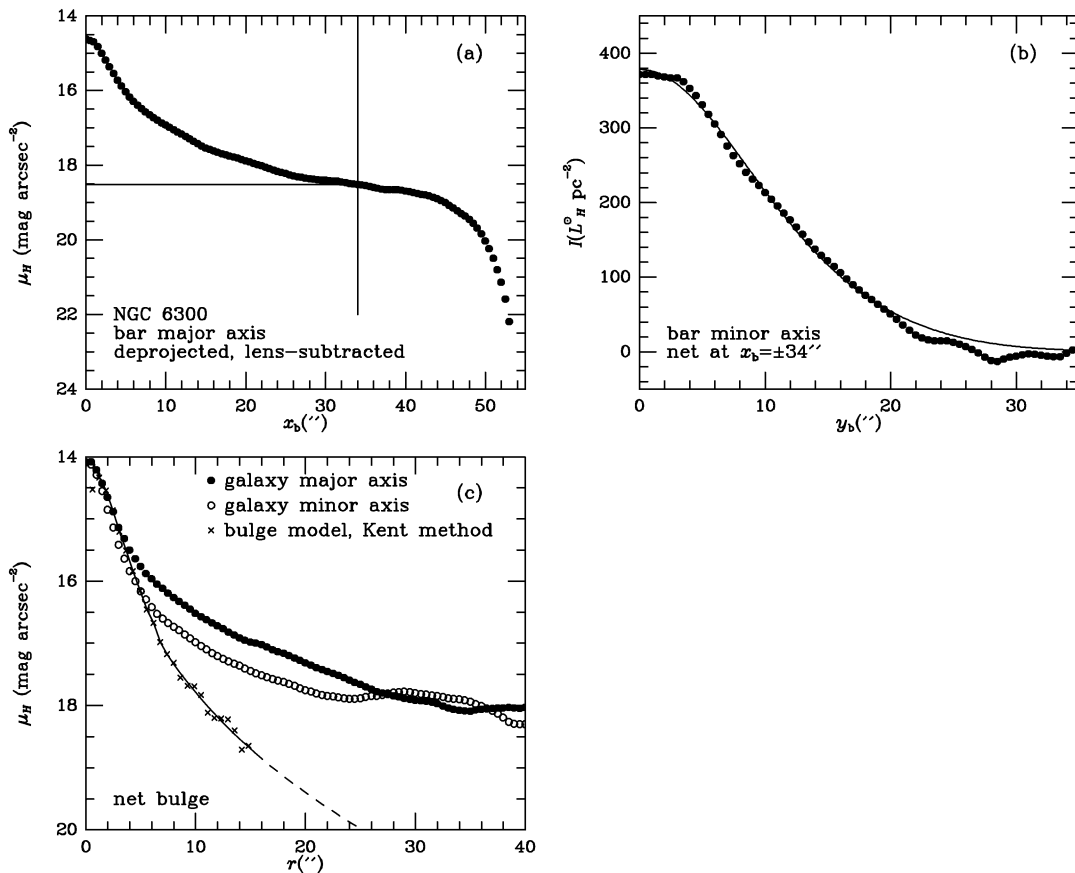


FIG. 18.—Photometric representations of the bar and bulge of NGC 6300 (see text): (a) Bar major-axis profile after subtraction of a constant lens surface brightness. The coordinate x_b is the radius along the deprojected bar axis, assuming an inclination of 52° and a line of nodes position angle of 108° . The vertical line refers to a reference radius, $x_b = 34''$, where the minor-axis profile of the bar was assumed to be uncontaminated by the bulge. The horizontal line shows the assumed surface brightness of the bar inside $34''$. (b) The net bar minor-axis profile, after subtraction of a constant lens surface brightness and averaged around the bar and on both sides of the nucleus. The coordinate y_b is the distance along an axis perpendicular to the bar. The solid curve is a double Gaussian fit to the profile for $y_b \leq 20''$ (see Table 2). (c) Profiles along the galaxy major and minor axes after removal of the primary bar as represented in (a) and (b). The crosses and solid and dashed curves represent a bulge model derived using the method of Kent (1986).

H -band luminosity. The bar model includes 5.6% of the total H -band luminosity. Both features are much less significant than in NGC 1433.

5.3. Fabry-Perot Velocity Field, Rotation Profiles, and Rotation Curve

The $H\alpha$ velocity field of NGC 6300 is shown in Figure 20. This shows that like NGC 1433, virtually no emission was detected from the bar region. However, B87 detected faint diffuse emission from this region. The lack of detection of this emission in the new RFP data is probably due to less sensitivity, owing to the cloudy conditions at the time of the observations. The concentration of $H\ II$ regions in the inner pseudoring/spiral zone was also shown by Ryder & Dopita (1993) and Crocker et al. (1996).

The slit spectroscopy of B87 provides a useful comparison with our new velocity field. B87 measured rotation profiles of NGC 6300 along eight position angles. To compare these with the FP data, we used bilinear interpolation to derive FP rotation profiles along the same position angles. These profiles were compared with B87's profiles by linearly interpolating values at the same radii. In general, we find very good agreement on the shapes of the rotation profiles between the two data sets. However, the FP velocities are on average 12 km s^{-1} lower than those in B87. Such a difference is not unusual for the RFP (as shown, e.g., by

Purcell 1998). Figure 21 compares the profiles after subtracting 12 km s^{-1} from B87's velocities. The most important finding from this analysis is that the new FP data confirm B87's finding that the apparent nucleus has a radial velocity significantly different from the systemic velocity. All of the rotation profiles are roughly symmetric around a systemic velocity nearly 100 km s^{-1} higher than that of the nucleus.

The dynamical parameters of NGC 6300 were derived using the Warner et al. (1973) method, as for NGC 1433, and the GAL program in the Astronomical Image Processing System (AIPS). The GAL routine (van Moorsel & Wells 1985) fits a parametrized rotation curve to the projected velocity field. We were particularly interested in determining the rotation center coordinates. However, since the bar region has little or no velocity information, we cannot derive the rotation center very reliably from the RFP data. The two methods gave the parameters listed in Table 7. With the nucleus included in the solutions, the two methods gave very consistent results on all five dynamical parameters. As found by B87, a mostly eastward offset is derived, although it is only half as large as that given by the long-slit data. Our estimates of the kinematic line of nodes and inclination compare very favorably with B87 and Ryder et al. (1996). B87 derived $\phi_n = 108^\circ \pm 1^\circ$ and $i = 52^\circ \pm 1^\circ$ using the full spectra and 103.5 ± 1.1 from the main part of the inner pseudoring region alone. From

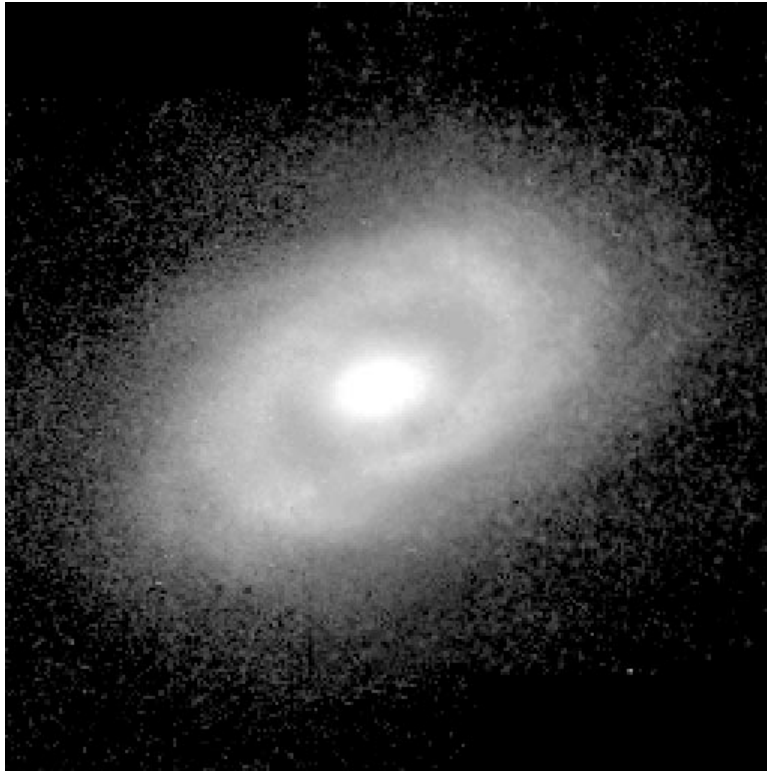


FIG. 19.—Sky plane H -band image of NGC 6300 with the primary bar (and also all foreground stars) subtracted. The contrast is set to show an inner oval whose shape and orientation are consistent with those of the outer disk isophotes. The field shown is $4'.86$ square. North is at the top, and east to the left.

Figure 17 of Ryder et al. (1996), the line of nodes from the H I kinematics averages $109^\circ \pm 2^\circ$ and the inclination averages $50^\circ \pm 3^\circ$ in the radius range $20''$ – $170''$. However, at the radius of the inner ring, the H I kinematic position angle drops to 105° . This fully agrees with the RFP result, which is dominated by the inner ring. For comparison, ellipse fits to outer isophotes gave a major-axis position angle of $108^\circ \pm 1^\circ$ and an inclination of $52^\circ \pm 2^\circ$.

The RFP data still favor an offset between the apparent nucleus of the galaxy and the rotation center, although it is less than that estimated by B87. No rotation center offset was found by Ryder et al. (1996), although their resolution may have been too low to detect it. Thus, if the velocity of the nucleus is due to rotational motion, then we must conclude that the rotation center of the gas disk in NGC 6300 is significantly displaced from the optical nucleus. This is



FIG. 20.—Fabry-Perot velocity field of NGC 6300. The color code is such that red corresponds to about 1250 km s^{-1} and purple corresponds to about 950 km s^{-1} . The field of view is $4'.88 \times 4'.12$, with north to the top and east to the left.

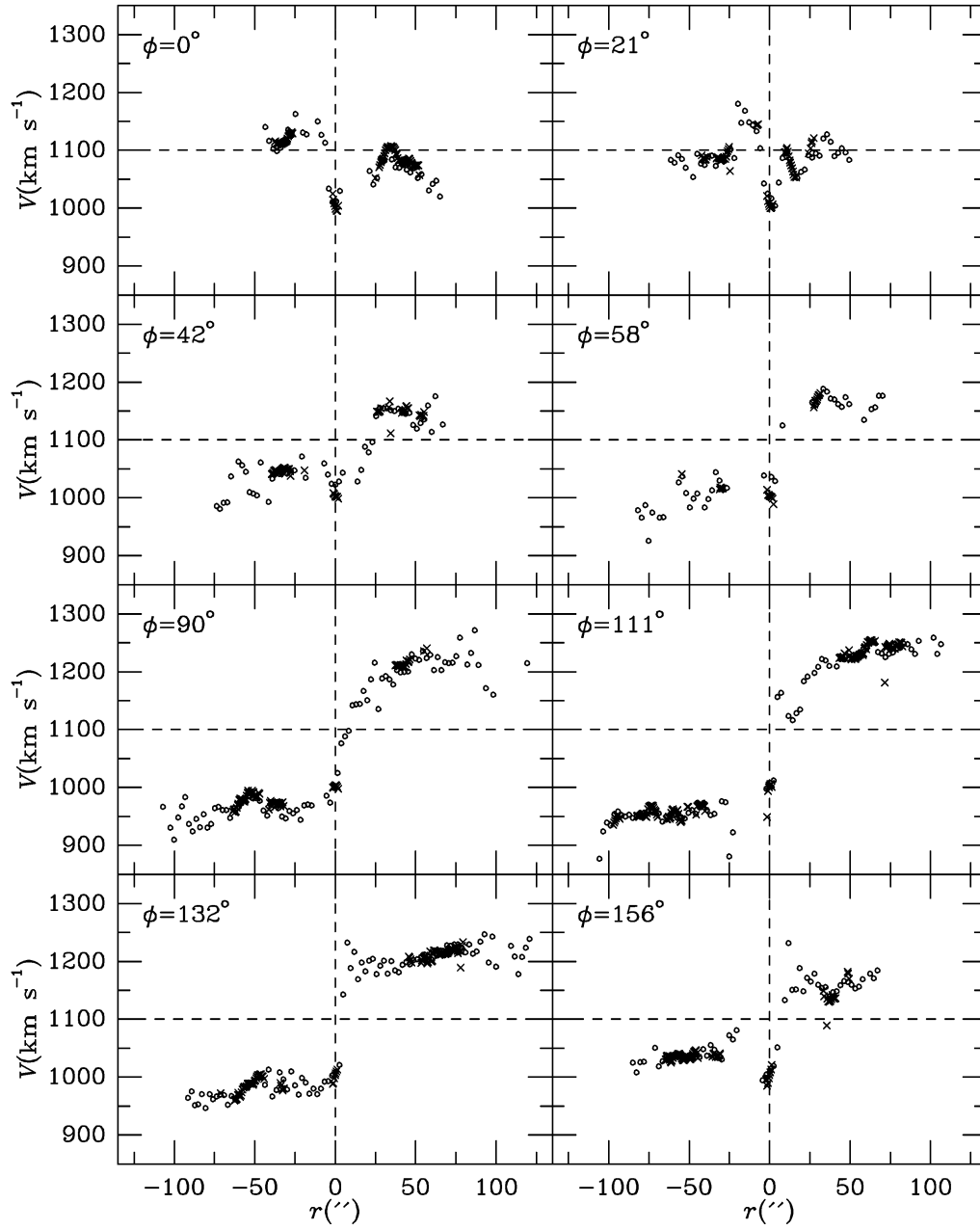


FIG. 21.—Comparison of radial velocity profiles of NGC 6300 from B87 and profiles interpolated from the velocity field in Fig. 20 along the same position angles. In making the comparison, a constant of 12 km s^{-1} has been subtracted from B87's velocities to account for a zero-point offset. Open circles show the reduced B87 values, while the crosses show the new RFP values.

TABLE 7
DYNAMICAL PARAMETERS FOR NGC 6300

Data Set	i (deg)	ϕ_n (deg)	V_s (km s^{-1})	$\Delta\alpha$ (arcsec)	$\Delta\delta$ (arcsec)	Method
RFP $H\alpha$	51 ± 2	104 ± 1	1100 ± 2	-2.5	-0.2	Warner et al. (1973), nucleus included
RFP $H\alpha$	50 ± 2	104 ± 1	1096 ± 2	$+0.9$	-0.2	Warner et al. (1973), nucleus excluded
RFP $H\alpha$	50.4	103.6	1100.3	-2.3	$+0.3$	van Moorsel & Wells (1985) GAL
Slit spectra (B87).....	52 ± 1	108 ± 1	1107 ± 5	-5.0	0.0	Warner et al. (1973)
Slit spectra (B87).....	52	103.5 ± 1.1	1116.6 ± 1.9	0.0	0.0	(V, ϕ) - diagram, inner ring only
H I (Ryder et al. 1996)	50 ± 3	109 ± 2	1109 ± 4	0.0	0.0	Begeman (1987) ROTCUR
Surface photometry (B87).....	51.6 ± 1.3	108 ± 1	Ellipse fits, outer isophotes

actually not without precedent. M31 has a double nucleus where the brighter component is offset from the dynamical center (see, for example, Lauer et al. 1993; Bacon et al. 1994). However, the size scale of the offset between the two systems is very different.

An alternative interpretation is that the velocities in the apparent nucleus of NGC 6300 are not due to rotational motions but to some kind of inflow or outflow, optical depth effect, or perhaps asymmetric or multiple but unresolved emission components. We have found no evidence for asymmetry or multiple components in the nuclear RFP H α profile in NGC 6300. Also, Busko & Steiner (1990) reported that high spectral resolution nuclear H α and [N II] λ 6584 profiles are symmetric. However, discrepancies between nuclear emission-line velocities and stellar systemic velocities have been found for many Seyfert galaxies. Nelson & Whittle (1995) measured [O III] and stellar systemic velocities for more than 50 Seyfert galaxies, and discrepancies of more than 100 km s⁻¹ in systemic velocities were found in a few cases, with a preference for the emission-line velocity to be less than the stellar velocity by -24 ± 8 km s⁻¹, on average. In contrast, H I and stellar systemic velocities were found to be in much better agreement by these authors. Similar differences were found by Keel (1996). These studies argue that we should be cautious about interpreting the nuclear velocity discrepancy in NGC 6300 as being solely due to an offset of the dynamical center of the gas distribution. If the offset is due to some non-rotational effect, we would have to reject the nucleus from consideration. Table 7 lists the dynamical parameters of NGC 6300 given by the Warner et al. method after excluding the nucleus. With nothing to constrain the solution close to the center, the method gives a rotation center offset nearly due west by 1". The offset is not significant, and the solution favors a rotation center coincident with the continuum nucleus.

The RFP velocity field favors the same inclination as that inferred from the H I velocity field, but gives a line of nodes 5° less than that derived from the H I velocity field in the inner regions. This discrepancy on ϕ_n probably is due to some noncircular motion, which is more averaged out by the large beam width in the H I data. Figure 22 shows that the rotation curves based on the RFP parameters are generally higher than those provided by the H I data by more than 20 km s⁻¹. However, if we recompute the RFP rotation curve fixing the orientation parameters to the H I averages, the discrepancy is reduced somewhat. The RFP rotation velocities nevertheless still average about 15 km s⁻¹ higher than the H I velocities for $r = 20''$ – $170''$. Ryder et al. (1996) found a similar discrepancy between the B87 rotation curve and the H I rotation curve. Some of the difference may be due to beam smearing, especially in the few inner most points (van Moorsel & Wells 1985). All of the final RFP rotation curves in Figure 22 are based only on velocity points within $\pm 45^\circ$ of the major axis, with points weighted by $\cos \theta$ as in Warner et al. (1973). Figure 22 also shows that for the indicated orientation parameters, the RFP rotation curve is not very sensitive to the slight possible offset of the rotation center from the nucleus. Also, there is general agreement with the rotation curve derived by B87.

For consistency, we will use in Paper II the RFP rotation curve based on the H I orientation parameters, with a rotation center offset of 2".4 east. This is compiled in Table 8 and shown as the filled circles in Figure 22.

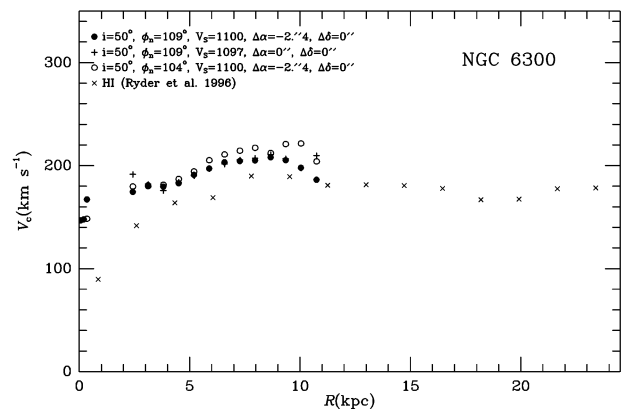


FIG. 22.—Rotation curve of NGC 6300. Rotation velocities based on the RFP velocity field are shown for different orientation parameters and rotation center offsets. The radius scale was set using a distance of 14.3 Mpc.

6. SUMMARY

We have presented new near-infrared and optical kinematic data on NGC 1433 and NGC 6300, two large and dissimilar southern ringed galaxies. The following are a few of the important findings from our detailed observational analysis:

1. The near-infrared structure of both galaxies still shows prominent pseudorings. Apart from a smoothness characteristic of the older stellar population, the near-infrared and blue light structures of both galaxies are very similar.
2. The inner structure of both galaxies can be interpreted in terms of a bar, a bulge, and a lens. In both cases, the minor-axis profile of the bar can be modeled as the sum of two Gaussian functions. After subtraction of the bar and lens components, the average bulge profile of NGC 1433 can be modeled in terms of a double exponential function.

TABLE 8

H α FABRY-PEROT ROTATION VELOCITIES IN NGC 6300^a

R (arcsec) (1)	$e(R)$ (arcsec) (2)	V_c (km s ⁻¹) (3)	$s.d.(V_c)$ (km s ⁻¹) (4)	$m.e.(V_c)$ (km s ⁻¹) (5)
1.0	1.0	146.6	18.7	4.4
3.0	1.0	147.8	12.7	1.7
5.0	1.0	167.1	20.3	5.6
35.0	5.0	174.5	17.6	0.7
45.0	5.0	180.9	20.9	0.3
55.0	5.0	179.5	18.4	0.2
65.0	5.0	182.8	14.0	0.2
75.0	5.0	190.9	13.8	0.2
85.0	5.0	197.1	12.6	0.2
95.0	5.0	203.4	9.9	0.2
105.0	5.0	204.4	9.4	0.3
115.0	5.0	205.0	8.4	0.3
125.0	5.0	208.0	12.4	0.5
135.0	5.0	205.2	9.3	0.4
145.0	5.0	198.1	10.2	0.9
155.0	5.0	186.3	10.6	2.4

^a Col. (1): radius along major axis; col. (2): radius range half-width; col. (3): mean rotation velocity; col. (4): standard deviation in mean rotation velocity; col. (5): mean error of mean rotation velocity.

3. Evidence has been presented that the bulges of both galaxies may be highly flattened either in the inner or the outer regions. Measurements of stellar absorption line velocities and velocity dispersions in the inner 7" radius of NGC 1433 give a ratio V_{\max}/σ about 1.8 times higher than that predicted for oblate spheroidal galaxy models flattened solely by rotation. In this region, the bulge of NGC 1433 is clearly a highly flattened, triaxial feature. After removal of the bar, the shapes of isophotes in the outer parts of the apparent bulge of NGC 6300 are very similar to the shapes of isophotes in the outer disk, suggesting that the outer bulge of NGC 6300 is also highly flattened.

4. Stellar rotation velocities in NGC 1433 show a turnover at $R \approx 7''$, consistent with the radius of maximum ellipticity in the triaxial part of the bulge. However, the stellar rotation velocity reached is only 60% that of the maximum gas rotation velocity in the inner ring region. We suggest that the difference is due mostly to asymmetric drift, caused by the steep density gradient and high velocity dispersion ($\sigma_c \approx 85 \text{ km s}^{-1}$) in the inner regions. Although we cannot make very accurate corrections for this effect, we show that the simplest assumptions bring the level of the stellar rotation curve to about the same rotation velocity as the atomic and ionized gas in the outer regions.

5. The composite rotation curve of NGC 1433, based on stellar, ionized gas, and atomic gas motions, is complete enough that we can derive Lindblad precession frequencies as a function of radius independent of any numerical model. For a pattern speed of $23 \text{ km s}^{-1} \text{ kpc}^{-1}$, the major-axis radius of the outer pseudoring extends to the outer Lindblad resonance; the average radius of the inner pseudoring coincides with the inner 4:1 ultraharmonic resonance; the sharp ends of the primary bar lie just inside this same resonance; the nuclear ring lies between two inner Lindblad resonances and closer to the inner of the two; and finally the average radius of the "plume" features lies close to the outer 4:1 ultraharmonic resonance. For the rings, these are

fairly standard interpretations (see Buta 1995 and references therein). In Paper II, we show that when the near-infrared light distribution is used to infer the gravitational potential in NGC 1433, we can reproduce much of its gaseous structure with a single pattern speed as above, again with standard resonance interpretations for the ring features.

6. Our new RFP observations of NGC 6300 confirm B87's original finding that the radial velocity of the nucleus of the galaxy is lower than the systemic velocity by nearly 100 km s^{-1} . B87 interpreted this as an effect of extinction, implying that the true nucleus is hidden by dust and that the rotation center of the gas disk is offset from the apparent nucleus. We have been able to definitively determine that dust is not significantly impacting the position of the nucleus of the galaxy, at least not to the extent that the rotation velocities require. We are not able to rule out the idea that the rotation center is actually offset from the nucleus, however we also suggest that there may be non-rotational motions in the Seyfert nucleus contributing to this effect.

R. B. would like to thank the Paris Observatory for a Temporary Visiting Astronomer position in the summer of 1998, which allowed this work to get started. R. B. would also like to acknowledge the contribution of the late David A. Allen, who served as the assistant astronomer at the AAT on the night of 1984 December 21, when the slit spectroscopy of NGC 1433 was obtained and the author had a serious accident. We also thank T. Williams and R. Schommer for assistance with the RFP observations and for many of the programs used for their reductions, and we thank the referee for many helpful comments. R. B. acknowledges the support of NSF grant AST 96-17154 to the University of Alabama for this work. G. M. and K. W. acknowledge the support of NSF Research Experiences for Undergraduates (REU) grant 94-24226, also to the University of Alabama.

REFERENCES

- Bacon, R., Emsellem, E., Monnet, G., & Nieto, J. L. 1994, *A&A*, 281, 691
 Baumgart, C. W., & Peterson, C. J. 1986, *PASP*, 98, 56
 Begeman, K. 1987, Ph.D. thesis, Univ. Groningen
 Bottema, R. 1993, *A&A*, 275, 16
 Busko, I. C., & Steiner, J. E. 1990, *MNRAS*, 245, 470
 Buta, R. 1984, *Proc. Astron. Soc. Australia*, 5, 467
 ———. 1986, *ApJS*, 61, 631
 ———. 1987, *ApJS*, 64, 383
 ———. 1995, *ApJS*, 96, 39
 Buta, R., & Combes, F. 1996, *Fundam. Cosmic Phys.*, 17, 95
 ———. 2000, in *ASP. Conf. Ser. 197, Dynamics of Galaxies: From the Early Universe to the Present*, ed. F. Combes, G. A. Mamon, & V. Charmandaris (San Francisco: ASP), 11
 ———. 2001, in preparation (Paper II)
 Buta, R., & Crocker D. A. 1993, *AJ*, 105, 1344
 Buta, R., Purcell, G. B., & Crocker, D. A. 1995, *AJ*, 110, 1588
 Caldwell, N., Kennicutt, R., Phillips, A. C., & Schommer, R. A. 1991, *ApJ*, 370, 526
 Crocker, D. A., Baugus, P. D., & Buta, R. 1996, *ApJS*, 105, 353
 Elias, J., Frogel, J. A., Matthews, K., & Neugebauer, G. 1982, *AJ*, 87, 1893
 Elmegreen, B. G. 1996, in *ASP Conf. Ser. 91, Barred Galaxies*, ed. R. Buta, D. A. Crocker, & B. G. Elmegreen (San Francisco: ASP), 197
 Elmegreen, B. G., & Elmegreen, D. M. 1985, *ApJ*, 288, 438
 Freeman, K. C. 1970, *ApJ*, 160, 811
 Hameed, S., & Devereux, N. 1999, *AJ*, 118, 730
 Harnett, J. I. 1987, *MNRAS*, 227, 887
 Illingworth, G. 1981, in *The Structure and Evolution of Normal Galaxies*, ed. S. M. Fall & D. Lynden-Bell (Cambridge: Cambridge Univ. Press), 27
 Keel, W. C. 1996, *ApJS*, 106, 27
 Kent, S. M. 1986, *AJ*, 91, 1301
 Kormendy, J. 1977, *ApJ*, 214, 359
 ———. 1982, *ApJ*, 257, 75
 Kormendy, J. 1993, in *IAU Symp. 153, Galactic Bulges* (Dordrecht: Kluwer), 209
 Kormendy, J., & Illingworth, G. 1983, *ApJ*, 265, 632
 Landolt, A. U. 1992, *AJ*, 104, 340
 Lauberts, A., & Valentijn, E. 1989, *The Surface Photometry Catalogue of the ESO-Uppsala Galaxies* (Garching: ESO)
 Lauer, T., et al. 1993, *AJ*, 106, 1436
 Maia, M. A. G., da Costa, L. N., & Latham, D. W. 1989, *ApJS*, 69, 809
 Malkan, M. A., Gorjian, V., & Tam, R. 1998, *ApJS*, 117, 25
 Mihalas, D., & Binney, J. 1981, *Galactic Astronomy* (New York: W. H. Freeman), chap. 7
 Mulchaey, J. S., Regan, M. W., & Kundu, A. 1997, *ApJS*, 110, 299
 Nelson, C. H., & Whittle, M. 1995, *ApJS*, 99, 67
 Phillips, M. M., Charles, P. A., & Baldwin, J. A. 1983, *ApJ*, 266, 485
 Purcell, G. B. 1998, Ph.D. thesis, Univ. Alabama
 Regan, M. W., & Mulchaey, J. S. 1999, *AJ*, 117, 2676
 Ryder, S. D., Buta, R. J., Toledo, H., Shukla, H., Staveley-Smith, L., & Walsh, W. 1996, *ApJ*, 460, 665
 Ryder, S. D., & Dopita, M. A. 1993, *ApJS*, 88, 415
 Salo, H., Rautiainen, P., Buta, R., Purcell, G. B., Cobb, M. L., Crocker, D. A., & Laurikainen, E. 1999, *AJ*, 117, 792
 Sargent, W. L. W., Schechter, P. L., Boksenberg, A., & Shorridge, K. 1977, *ApJ*, 212, 326
 Simien, F., & de Vaucouleurs, G. 1986, *ApJ*, 302, 564
 Tonry, J., & Davis, M. 1979, *AJ*, 84, 1511
 Tully, R. B. 1988, *Nearby Galaxies Catalogue* (Cambridge: Cambridge Univ. Press)
 Tully, R. B., Pierce, M. J., Huang, J.-S., Saunders, W., Verheijen, M. A. W., & Witchalls, P. L. 1998, *AJ*, 115, 2264
 van der Kruit, P. C., & Freeman, K. C. 1986, *ApJ*, 303, 556
 van Moorsel, G., & Wells, D. C. 1985, *AJ*, 90, 1038
 Warner, P. J., Wright, M. C. H., & Baldwin, J. E. 1973, *MNRAS*, 163, 163
 Wozniak, H., Friedli, D., Martinet, L., Martin, P., & Bratschi, P. 1995, *A&AS*, 111, 115